Front passivation of Cu(In,Ga)Se_2 solar cells using Al_2O_3: Culprits and benefits

M. A. Curado[a,b,*], J. P. Teixeira[a], E. F. M. Ribeiro[b], R. C. Vilão[b], H. V. Alberto[b], J. M. V. Cunha[a,c,d], T. S. Lopes[a,e,f,g], K. Oliveira[a], O. Donzel-Gargand[a,h], A. Hultqvist[h], S. Calderon[a], M. A. Barreiros[i], W. Chiappim[c,d], J. P. Leitão[c,d], M. Monteiro[a,j], A. G. Silva[j], T. Prokscha[k], C. Vinhais[a,l], P. A. Fernandes[a,d,l], P. M. P. Salomé[a,c]

[a]*INL,International Iberian Nanotechnology Laboratory, 4715-330 Braga, Portugal*
[b]*University of Coimbra, CFisUC, Department of Physics, R. Larga, P-3004-516 Coimbra, Portugal*
[c]*Departamento de Física, Universidade de Aveiro, Campus Universitário de Santiago, 3810-193 Aveiro, Portugal*
[d]*i3N, Universidade de Aveiro, Campus Universitário de Santiago, 3810-193 Aveiro, Portugal*
[e]*Institute for Material Research (IMO), Hasselt University (partner in Solliance), Agoralaangebouw H, Diepenbeek, 3590, Belgium*
[f]*Imec division IMOMEC (partner in Solliance), Wetenschapspark 1, 3590 Diepenbeek, Belgium*
[g]*EnergyVille 2, Thor Park 8320, 3600 Genk, Belgium*
[h]*Solar Cell Technology, Department of Materials Science and Engineering, Uppsala University, Box 534, SE-75121 Uppsala, Sweden*
[i]*Laboratório Nacional de Energia e Geologia, Estrada do Paço do Lumiar 22, Lisboa, Portugal*
[j]*Departamento de Física, Faculdade de Ciências e Tecnologia, Universidade Nova de Lisboa, Campus de Caparica, 2829-516 Caparica, Portugal*
[k]*Laboratory for Muon Spin Spectroscopy, Paul Scherrer Institute, CH-5232 Villigen PSI, Switzerland*
[l]*CIETI, Departamento de Física, Instituto Superior de Engenharia do Porto, Instituto Politécnico do Porto, Porto 4200-072, Portugal*

Abstract

In recent years, the strategies used to break the Cu(In,Ga)Se_2 (CIGS) world record of light to power conversion efficiency, were based on improvements of the absorber optoelectronic and crystalline properties, mainly using complex post-deposition treatments. To reach even higher efficiency values, advances in the solar cell architecture are needed focusing in the CIGS interfaces. In this study, we evaluate the structural, morphological and optoelectronic impact on the CIGS properties of using an Al_2O_3 layer as a potential front passivation layer. The impact of Al_2O_3 tunnelling layer between CIGS and CdS is also addressed in this study. Morphological and structural analyses reveal that the use of Al_2O_3 alone is not detrimental to CIGS, although it does not resist to the CdS chemical bath deposition. When CdS is deposited on top of Al_2O_3, the CIGS optoelectronic properties are heavily degraded. Nonetheless, when Al_2O_3 is used alone, optoelectronic measurements reveal a positive impact of its inclusion such as a very low concentration of interface defects and the CIGS keeping the same recombination channels. With the findings of this study the best use of Al_2O_3 front passivation layer could be with alternative buffer layers. The Al_2O_3 layer will keep the CIGS surface with a low density of defects while keeping its structural and optoelectronic properties as good as the ones when CdS is deposited. It can also be reported that a comparison between the different analyses allowed us to strongly suggest for the first time that low-energy muon spin spectroscopy (LE-μSR) is sensitive to both charge carrier separation and bulk recombination in complex semiconductors.

DOI: https://doi.org/10.1016/j.apmt.2020.100867

Keywords: surface passivation; Al_2O_3; $Cu(In,Ga)Se_2$ (CIGS), thin film solar cells, atomic layer deposition (ALD)

1. Introduction

With a world record of light to power conversion efficiency value of 23.35 % and a significant number of advantages over other photovoltaic technologies [1,2], $Cu(In,Ga)Se_2$ (CIGS) thin film solar cells will play a key technological role in the energy sector. Over the past years, there has been an increasing focus on the improvement of the CIGS interfaces. In detail, two different approaches have been introduced for optimization of the CIGS interfaces: 1) the incorporation of a passivation dielectric layer on the rear [3–6] or on the front surfaces [7,8] and, 2) a surface reconstruction treatment via alkaline deposition also known as post deposition treatment (PDT) [9–12]. For the rear interface, the use of a dielectric nano-patterned layer as a point contact structure has proven to reduce interface recombination [5,13,14] by two means: 1) reducing the density of the interface active defects, i.e. chemical passivation [6,15], and 2) repelling minority carriers by a built-in electrical field due to fixed charges at the dielectric surface [16–18]. While this approach has been successfully implemented in the rear contact, the front contact has been mostly improved using alkali post deposition treatments [9,19,20], However, it is still heavily debated its full effects and if benefits are due to bulk recombination changes [21–24]. In PDT processes, after the CIGS deposition, a fluorine-alkali compound is evaporated on the CIGS, leading to several optoelectronic changes that improve device performance [23,25,26]. In any case, it should be noted that some of the benefits of this process are related to the thinning down of the CdS buffer layer [9,27,28], improvements in the CIGS doping [29–31] and on the CIGS grain boundaries [21,32,33], leaving extra room for improvement in the actual CIGS interface. Moreover, the industrial application of PDT treatments is complex and can hinder the technological development, hence, other advances are also needed. The PDT approach has also benefited from the fact that its deposition does not cause any CIGS surface damage as other deposition methods, such as sputtering, are known to cause CIGS surface damage [34,35]. Such surface sensitivity increases the requirements to understand what compound can be deposited on CIGS, and most importantly its deposition conditions. Hence, for CIGS front interface passivation there is the need to find additional passivation processes and materials that leave the surface pristine and that can lower the effects of interface recombination.

Preliminary tests of dielectric passivation on chalcogenides front surface have been studied [7,8,36]. However, no significant improvements in the CIGS device performance were observed [7,8] suggesting that a fundamental understanding of the dielectric physical properties and the impact of those layers on the CIGS optoelectronic properties are still needed. Simulation studies have shown that CIGS devices with both passivated interfaces can increase its power conversion efficiency between 3.4 % (abs) [37] up to 7 % (abs) [38], compared with non-passivated devices [37] demonstrating the unexplored potential of front interface passivation in this type of devices.

Based on the improvements seen for interface optimization of the rear dielectric passivation, the theoretical studies showd significant gains in device performance in front passivation devices. In this contribution, it will be studied in detail the impact of Al_2O_3 deposition layers on the CIGS surface using atomic layer deposition (ALD). Al_2O_3 was chosen since it has been widely studied as rear interface passivation material [39,40]. Moreover, as it is known that both sputtering [41] and high temperature depositions [42,43] lead to CIGS surface damage, mostly via elemental intermixing and composition changes, ALD will be used as it is widely used for the deposition of CdS alternative buffer layers [44–46]. ALD allows for a low temperature deposition with low kinetic energy [47], conditions that minimize surface damage. To infer the effects of the dielectric ALD deposition, several structural, chemical and optoelectronic characterization techniques were used and showed that the Al_2O_3 ALD deposited layer is a promising candidate to be used in CIGS front passivation as demonstrated by the low density of interface defects (D_{it}) and the muon spin spectroscopy that demonstrate the beneficial impact of the Al_2O_3. We also identified that the deposition of CdS on top of Al_2O_3 can be problematic as the basic chemical bath deposition attacks the Al_2O_3 layer.

2. Experimental details

2.1. Sample fabrication

In this study, the CIGS layer has a linear Ga profile, which is commonly associated with reducing rear interface recombination, allowing for a higher impact of the front passivation layer in the recombination mechanisms [48]. The CIGS thickness is 2.0 µm with [Cu]/([Ga] + [In]) = 0.92 ± 0.01 (CGI) and [Ga]/([Ga] + [In]) = 0.41 ± 0.02 (GGI) as measured by X-ray fluorescence. Soda-lime-glass/Molybdenum (Mo)/CIGS stacks were used. The different deposition methods for the layers are described elsewhere [49]. After growing the CIGS, the substrates were cut into four pieces, and each one received a different treatment: i) a chemical bath deposition (CBD) CdS layer (Ref sample); ii) an ALD 50 cycles Al_2O_3 layer ($Al_2O_3$50 sample); iii) an ALD 250 cycles Al_2O_3 layer ($Al_2O_3$250 sample); and iv) an ALD 50 cycles Al_2O_3 layer followed by a CBD CdS (Al_2O_3/CdS sample). A conventional CdS layer was deposited through a 60 ºC CBD, according to [49] on the Ref and Al_2O_3/CdS samples. The Al_2O_3 layers were deposited through ALD, on Picosun R200 reactors, using trimethylaluminum (TMA) and water (H_2O) as precursors of Aluminium (Al) and Oxygen (O), respectively. Each ALD cycle followed the sequence of exposing: TMA during 0.1 s, Nitrogen (N_2) purge for 8 s, H_2O for 0.1 s and another N_2 purge during 20 s. The substrate temperature in this study was 100 ºC to further minimize surface damage, although it may influence the crystal quality of the deposited layer. Moreover, quartz substrates were used to determine the thickness of the Al_2O_3 layers, keeping the same conditions as the ones used in the CIGS samples. The deposition of 50 and 250 cycles provided 5 and 25 nm Al_2O_3 layers, respectively, as measured using X-ray reflectivity. These values will be considered as the nominal thickness of the Al_2O_3 layer on the CIGS samples. A summary of the structure of the samples and the deposition method of the top layer is presented in Table 1. The samples were divided into two sets. The first set of samples was used to perform Raman spectroscopy, grazing incident X-Ray diffraction (GIXRD), X-Ray diffraction (XRD), scanning transmission electron microscopy (STEM) with energy-dispersive X-ray spectroscopy (EDS), X-Ray Photoelectron Spectroscopy (XPS) and time resolved photoluminescence (TRPL). The second set was used for low-energy muon spin spectroscopy (LE-µSR), photoluminescence (PL), and later, Al circular contacts (thickness of 400 nm) with a diameter of 1 mm were deposited through thermal evaporation, to perform electrical measurements. For the µSR measurements the Ref sample was split into two pieces and the CdS layer was removed with a Hydrochloric acid (HCl) treatment (10%), then it was immediately transferred to a N_2 environment, to avoid surface oxidation.

Table 1. Name of the samples used in this study and its description. Besides a CIGS/CdS sample (Ref), the other three samples have different combinations of ALD-deposited Al_2O_3 and CdS.

Sample Name	Colour plot	Structure	Note
Ref		CIGS/CdS	Typical CIGS/CdS sample.
$Al_2O_3$50		CIGS/Al_2O_3	50 cycles of Al_2O_3, nominal thickness of 5 nm.
$Al_2O_3$250		CIGS/Al_2O_3	250 cycles of Al_2O_3, nominal thickness of 25 nm.
Al_2O_3/CdS		CIGS/Al_2O_3/CdS	50 cycles of Al_2O_3, nominal thickness of 5 nm. Standard CdS deposition.

2.2. Characterization Methods

Structural and morphological properties of the samples were characterized by Raman spectroscopy, GIXRD, XRD, STEM-EDS and XPS. Raman spectroscopy was performed using a Witec Alpha 300R Raman System equipped with a green laser (λ=532 nm). The laser excitation power was 1 mW and a lens focus of 100x. Each sample was measured at least on three different spots with an exposition time of 5 s, and for simplicity representative plots will be shown and discussed. GIXRD patterns were recorded with a BRUKER D8 Advance diffractometer at a grazing incidence angle of 0.35º and Copper (Cu) K_α (λ=1.5406 Å) as the radiation source. XRD was performed on an XRD PANalytical XPert Pro equipped and Cu K_α, using the Bragg Brentano configuration. STEM images were taken with a FEI Titan ChemiSTEM Cs-probe corrected TEM, operating at 200 kV. The lamella were prepared by focused ion beam (FIB) in a FEI Dual-Beam Helios 450S using Mo-grids. On top of the samples, prior to the preparation, a protective evaporated Carbon (C) layer followed by a Platinum (Pt) bi-layer was deposited using the electron beam and the Gallium (Ga) beam [50]. To perform the EDS maps, the following elements and their corresponding emission spectrum line were chosen: O K_α=0.525, Al K_α=1.487, S K_α=2.309, Cadmium (Cd) L_α=3.132, Cu K_α=8.040, Ga K_α=9.241, Selenium (Se) K_α=11.207 and Indium (In) K_α = 24.210 keV. The XPS system ESCALAB 250 Xi Thermo Scientific is equipped with a monochromatic Al K_α source. For the depth profile analysis, the sputter source was an ion Argon beam with an ion current of 10 mA and an energy of 2000 eV. For the circuit-fitting, capacitance-conductance-frequency (C-G-f) measurements were conducted using a precision LCR meter Agilent E4980 A. The measurements were performed in dark, at room

temperature, with 30 mV (V_{RMS}), 0 V bias and a frequency range from 20 Hz to 1 MHz. Capacitance-voltage-frequency (C-V-f) measurements were also conducted in dark, at room temperature, with 30 mV (V_{RMS}), a frequency of 10 kHz and a bias range between -5 V and 1 V. Light soaking at AM1.5 was performed during 20 min on all samples with cooling of the substrate to 20 ºC, prior to the measurements. Low temperature PL measurements were performed in a Bruker Vertex 80v Fourier Transform Infrared (FTIR) spectrometer, equipped with an InGaAs detector. The light source was a 532 nm diode-pumped solid-state (DPSS) laser. The laser power was measured at the front of the spectrometer window (spot diameter of ≈ 1 mm). TRPL was performed with a photo spectrometer from Picoquant with a TimeHarp 260 single photon counter. A λ=532 nm laser, with an excitation approximately of 0.1 Wcm^{-2}, with a repetition rate of 3 MHz was used. The μSR measurements were performed at the μE4 beam line of the Swiss Muon Source [51], at the Paul Scherrer Institute (PSI), using the low energy muon instrument LEM. Positive muons were implanted in the samples in the presence of an external magnetic field B=10 mT, using transverse field geometry, at a fixed temperature of 40 K and variable implantation energy, between 3 and 26 keV, in order to perform depth dependent studies.

3. Results and Discussion

Novel approaches to implement front passivation layers on CIGS, require fundamental studies to understand the possible changes from the CIGS surface to the bulk physical properties and in order to study Al_2O_3 as front passivation, such studies are presented in this work. For clarification purposes, in this study, the bulk terminology was adopted to discuss the CIGS properties that are located several tens of nm's away from the CIGS surface. First, it was carefully investigated if structural changes occur that might be due to the ALD temperature and evaluate the possibility of elemental diffusion into CIGS due to Al_2O_3 deposition. Afterwards, a complementary optoelectronic study was performed in order to understand the Al_2O_3 influence on the CIGS electronic structure. In order to have a fair and proper comparison between samples, the same CIGS substrate was cut into four pieces that allowed a comparison between the different samples as described in the Fig. 1.

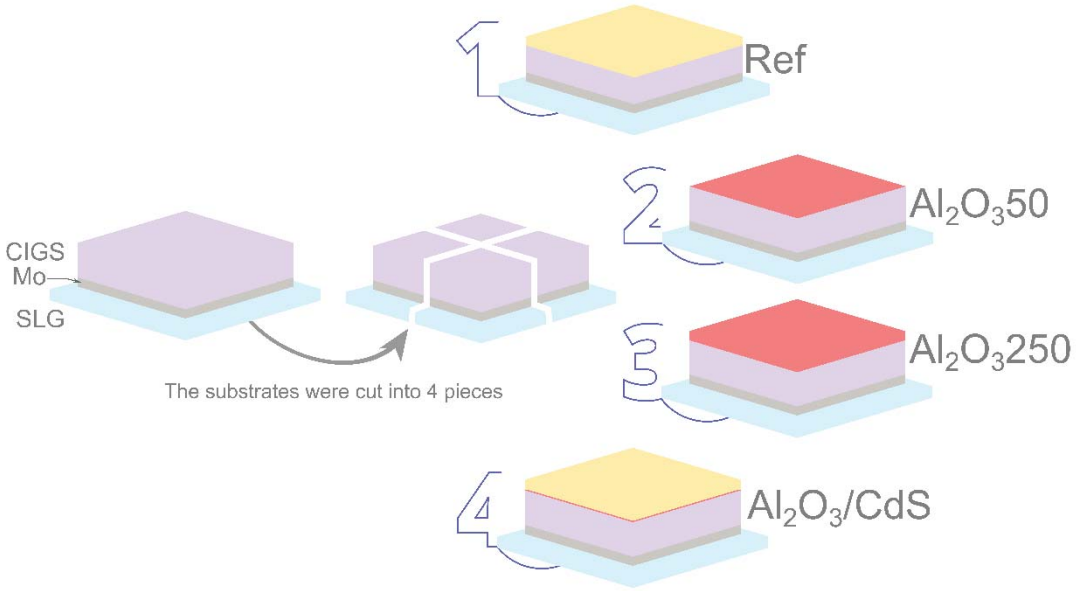

Fig 1: Schematic representation of the samples used in this work. The same CIGS piece was used for the four different samples: 1) CBD CdS layer (Ref sample); 2) an ALD 50 cycles Al_2O_3 layer ($Al_2O_3$50 sample); 3) an ALD 250 cycles Al_2O_3 layer ($Al_2O_3$250 sample); and 4) an ALD 50 cycles Al_2O_3 layer followed by a CBD CdS (Al_2O_3/CdS sample).

3.1 Structural Characterization

From the Raman analysis, (Fig. 2), all samples exhibit a sharp peak at 176 cm^{-1}, linked to the A_1 symmetry CIGS mode [52] and a broader peak at 217 cm^{-1} that is associated to CIGS B_2/E symmetry [53]. For the samples containing the CdS layer, a peak related to this compound is additionally observed at 300 cm^{-1} [54]. The CdS peak has quite different shapes in the two samples, being the one of the Al_2O_3/CdS sample broader than the one observed for the Ref sample, evidenced by the asymmetric shape of its peak. Such a discrepancy may indicate

that the two CdS layers do not have the same structural properties. However, such asymmetry at the lower energy side could also come from the presence of $Cu_{2-x}Se$ that has a Raman peak at 260 cm^{-1} [55]. It can be noted that no signal associated with the ordered vacancy compound (OVC) phase [56] was detected, in any of the studied samples. Since no noteworthy secondary phases were detected, the CIGS composition and crystal quality will be evaluated using a pseudo-Voight function to fit the A_1 peak. The obtained values of the peak position (X_c) and the full width at half maximum (FWHM) are presented in the inset table in Fig. 2. All samples have the A_1 peak centred in the range 176.2-176.6 cm^{-1}, a variation that is within instrumental error. Despite the different passivation strategy applied on CIGS, the scrutinized CIGS layers are structurally identical for the different samples, which is further supported by the similar magnitude FWHM values obtained for these samples. This might suggest that the deposition of Al_2O_3 does not change the near surface region of the CIGS in crystallographic terms or the differences are too small to be detected by Raman scattering.

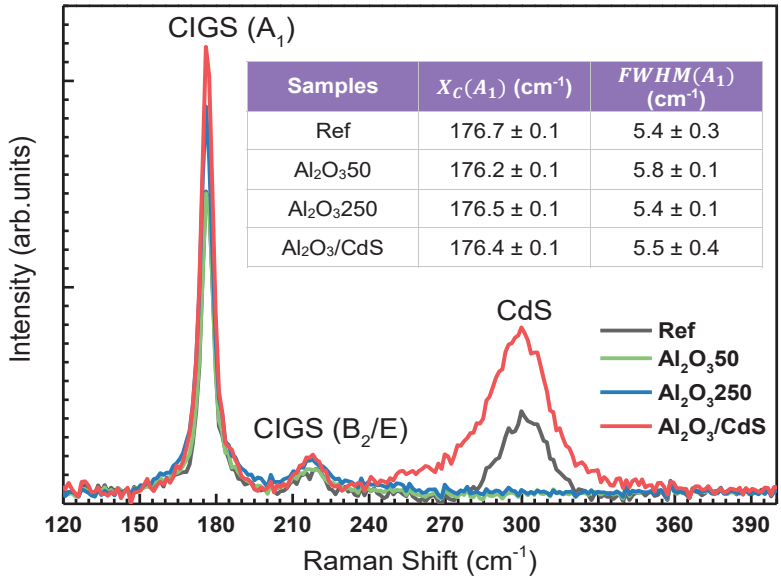

Samples	$X_C(A_1)$ (cm^{-1})	$FWHM(A_1)$ (cm^{-1})
Ref	176.7 ± 0.1	5.4 ± 0.3
Al_2O_350	176.2 ± 0.1	5.8 ± 0.1
Al_2O_3250	176.5 ± 0.1	5.4 ± 0.1
Al_2O_3/CdS	176.4 ± 0.1	5.5 ± 0.4

Fig. 2: Raman spectra of the studied samples. No significant changes in the CIGS peaks were detected. However, the Al_2O_3/CdS sample has a slightly different CdS peak with an asymmetry at the lower wavenumber side of its 300 cm^{-1} peak. Values and fitting errors of X_c and FWHM obtained from the pseudo-Voight function fit to the A_1 symmetry CIGS are shown in the table inset.

Since Raman spectroscopy only allows for a near surface analysis and somewhat localized in area, GIXRD and XRD measurements were performed to complement the Raman structural characterization of the CIGS layer. The GIXRD diffractograms of the Al_2O_350, Al_2O_3250, and Al_2O_3/CdS samples are shown in Fig. 3 a). The CIGS diffraction peaks related to the (112) and (220)/(204) reflections are present in all studied samples. However, the diffraction peaks related to CIGS planes (103) and (211) are only clearly visible for the Al_2O_350 and Al_2O_3250 samples. None of the samples present any peak linked to the Al_2O_3 as expected due: i) the low thickness value of the Al_2O_3 layer, and ii) the amorphous structure of the Al_2O_3 layer. The latter hypothesis is supported by S. Gieraltowska *et al.*, where it is shown that growing dielectric films with a temperature below 100 ºC and a thickness lower than 200 nm, gives origin to amorphous films [57]. Note that the studied Al_2O_3 layers were deposited at 100 ºC and their nominal thicknesses are much lower than 200 nm (5 and 25 nm). Moreover, crystalline Al_2O_3 films through ALD are usually prepared at temperature values higher than 600 ºC [58].

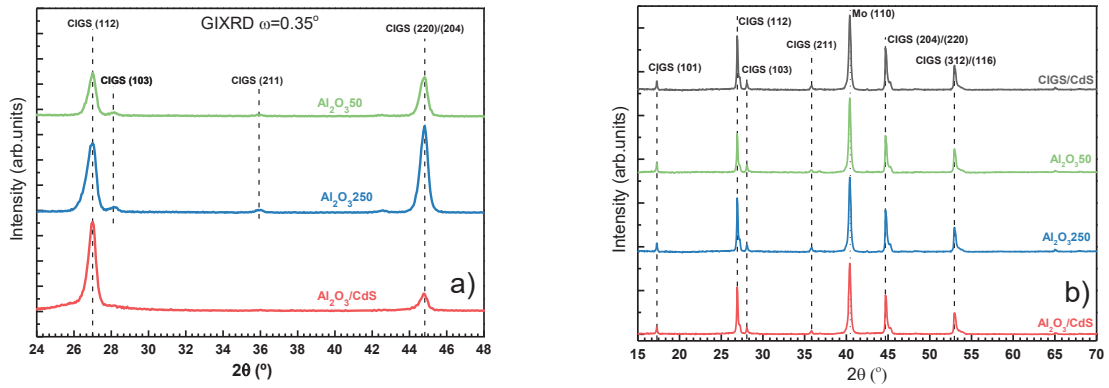

Fig. 3: a) GIXRD diffractograms of the $Al_2O_3$50, $Al_2O_3$250, and Al_2O_3/CdS samples, with an incident angle ω=0.35 °. CIGS diffraction peaks (112) and (220)/(204) are visible in all the samples, but the (103) and (211) reflections are only detectable in the $Al_2O_3$50 and $Al_2O_3$250 samples. b) XRD of the studied samples showing no visible differences among them, highlighting the fact the different top layers depositions did not change the CIGS bulk structural properties.

Table 2: Intensity ratios of the GIXRD CIGS peak of the crystalline plane (220)/(204) and XRD CIGS peaks of the crystalline plane (112), (220)/(204) and (312). Comparison with a powder database of CuInSe2 [59].

Sample	**Intensities Ratios**			
	$I_{112}/I_{(220/204)}$		**I_{112}/I_{312}**	**I_{204}/I_{312}**
Powder (Database)	1.75		3.43	1.96
	GI-XRD	**θ-2θ XRD**	**θ-2θ XRD**	**θ-2θ XRD**
Ref	-	1.29	2.20	1.71
$Al_2O_3$50	1.10	1.05	1.64	1.57
$Al_2O_3$250	0.79	0.89	1.42	1.60
Al_2O_3/CdS	5.31	1.21	2.20	1.83

To compare structural changes occurring in the CIGS near surface region with bulk, θ-2θ XRD measurements were also performed (Fig. 3 b). All XRD diffractograms show several diffraction peaks unequivocally related to the CIGS crystalline phase. The position and shape of the several peaks are similar between the samples, likely indicating that there are no CIGS bulk differences caused by the Al_2O_3 and the CdS depositions. Pseudo-Voight fits of selected GIXRD and XRD peaks were performed to estimate the preferential crystal orientation, following the procedure described elsewhere [60], and the obtained intensity ratios are presented in Table 2. The GIXRD analysis reveals structural differences in the Al_2O_3/CdS sample, when comparing with the samples that only contain Al_2O_3. For the Al_2O_3 samples, the $I_{112}/I_{(220/204)}$ GIXRD and XRD values are close, indicating that there are no significant differences between the surface and the bulk. However, for the Al_2O_3/CdS sample, the same GIXRD ratio (5.31) is extremely different than the XRD one (1.21). Such results suggest that the Al_2O_3/CdS sample surface is somewhat different than its bulk, and different from the other samples. Although the Raman results showed differences in the CdS layer for this sample, both the XRD and the Raman analysis tend to indicate that this sample has some crystal difference at its surface than the other samples. Additionally, neither GIXRD nor XRD analysis showed the presence of any secondary phases.

High-angle annular dark field (HAADF) STEM images (Fig. 4) show conformal layers without pinholes or any other artefacts. The Ref sample (Fig. 4 a)), shows the CIGS and CdS layers, and an additional protective layer, composed by C, which is used for the lamella preparation. The $Al_2O_3$50 and $Al_2O_3$250 samples are presented in Fig. 4 b) and c), respectively, where it is possible to distinguish the CIGS and a thin Al_2O_3 layer indicating a conformal growth of both Al_2O_3 layers. It should be noted that for the $Al_2O_3$50, as the layer is quite thin, the Al_2O_3 conformity might not be as perfect as the one clearly found for the three other samples. An ImageJ analysis of a large group of images provides an Al_2O_3 layer average thickness value of 4.3 and 22 nm (see Table 3) which are in good agreement with the nominal 5 and 25 nm for the $Al_2O_3$50 and $Al_2O_3$250 samples, respectively. For the sample Al_2O_3/CdS, (Fig. 4 d)), it was expected to observe both the Al_2O_3 and the CdS layers. Nonetheless, only the CdS layer is clearly visible. Comparing the morphological properties and thickness of the CdS layer in the

samples that contain this layer (Fig. 4 a) and 4 d)), the CdS thickness of both samples is similar. However, the CdS layer presents a porous morphology in the Al_2O_3/CdS sample, which is compatible with the broader CdS peak observed for this sample in the Raman spectrum.

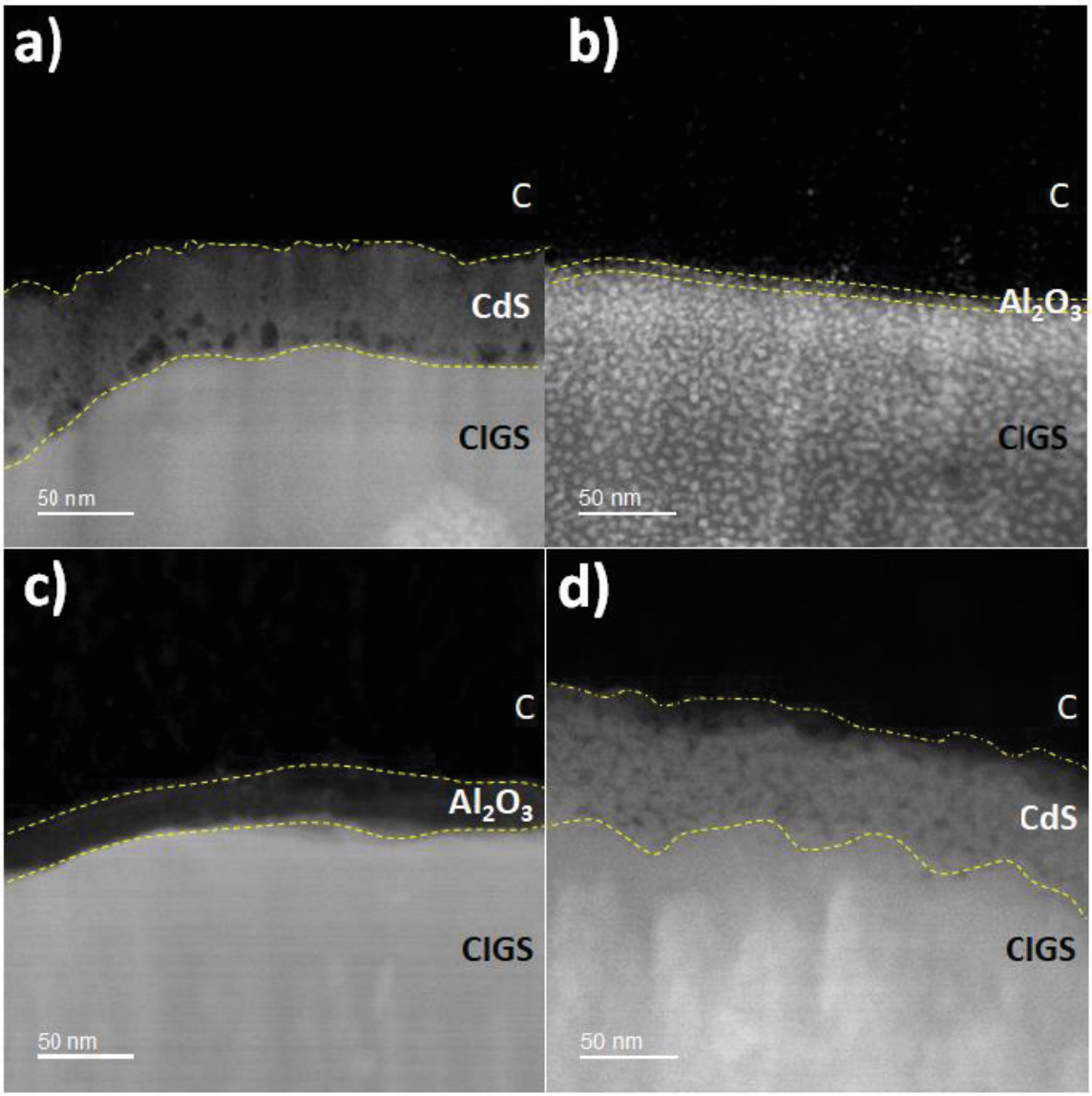

Figure 4: HAADF STEM images of the final lamella a) Ref b) $Al_2O_3$50, c) $Al_2O_3$250, and d) Al_2O_3/CdS samples. It is not visible the Al_2O_3 layer on Al_2O_3/CdS. All samples show the protective carbon layer on top.

Table 3 : Comparison between the measured thickness values obtained for the Al_2O_3 layers on quartz substrates and the average and standard deviation thickness values estimated by ImageJ for the Al_2O_3 layers on SLG/Mo /CIGS substrate, being also presented the thickness values of the CdS layers grown over the latter substrate.

Sample	Al_2O_3 nominal thickness (nm)	Al_2O_3 thickness (nm)	CdS thickness (nm)
Ref	-	-	54 ± 3
Al_2O_3 50	5	4.3 ± 0.2	-
Al_2O_3 250	25	22 ± 4	-
Al_2O_3/CdS	5	-	54 ± 7

To understand the absence of the Al_2O_3 layer on the Al_2O_3/CdS sample, two EDS analyses were performed. The STEM-EDS elemental mapping performed on the $Al_2O_3$250 sample, Fig. 5, reveals two distinct layers, the Al_2O_3 and the CIGS layer. An overlap between the Al K_α and Se L_α peaks (1.486 and 1.379 keV, respectively) hinders an unambiguous determination of the Al_2O_3 layer. However, when the Cu signal is superimposed to the Al one

(Fig. 5 a')) a defined interface compatible with the O EDS distribution (Fig. 5 b)) is observed, clearly showing: i) the existence of an Al_2O_3 layer and, ii) a defined interface. The EDS line profiles follow the same trend and they show that there is a peak in the Al signal in the same position as the O peak, which is a further evidence of the presence of the Al_2O_3 layer at the CIGS surface. According to the EDS analysis, there is no indication of elemental diffusion between the CIGS and the Al_2O_3, as it might occur in some cases, between the CIGS and CdS [50,61–63].

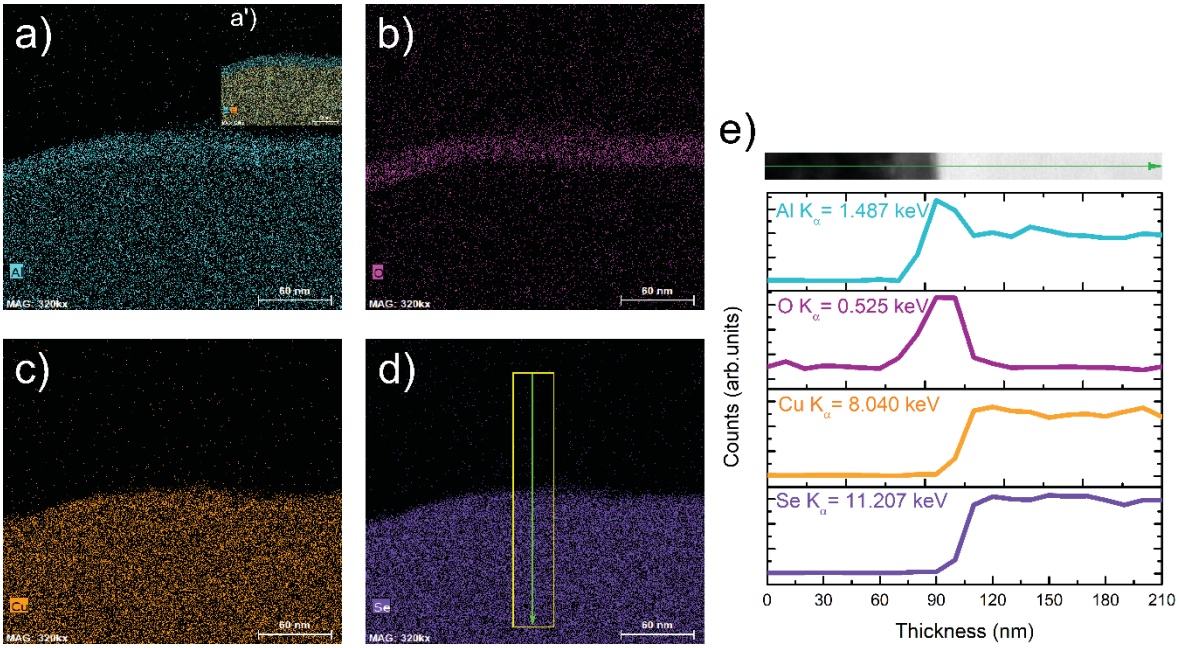

Fig. 5: STEM-EDS mapping of the $Al_2O_3$250 sample: Full EDS mapping of (a) Al, (a') Al-Cu, (b) O, (c) Cu, and (d) S. (e) EDS line profiles for all the Al, O, Se and Cu. The green arrow corresponds to the EDS linescan region.

To confirm the absence of the Al_2O_3 layer in the Al_2O_3/CdS sample, as observed by the STEM image, the EDS elemental distribution and an EDS scanline analysis were also performed (Fig. 6). The Al signal appears in the same region as the CIGS layer due to the overlap with Se, already discussed (Fig. 6 e)). Note that for the $Al_2O_3$250 sample, the O layer was clearly observed in conjugation with the increased Al signal. However, for Al_2O_3/CdS sample the O distribution is constant, hinting to the absence of the Al_2O_3 layer, (Fig. 6 e)). The Se EDS line profiles follow the same trend in the CIGS layer and the Al signal just follows the Se one, also contrary to the previous analysis where a clear increase of the Al signal was observed. Hence, the combined STEM and EDS analysis confirm the absence of an Al_2O_3 layer in the Al_2O_3/CdS sample.

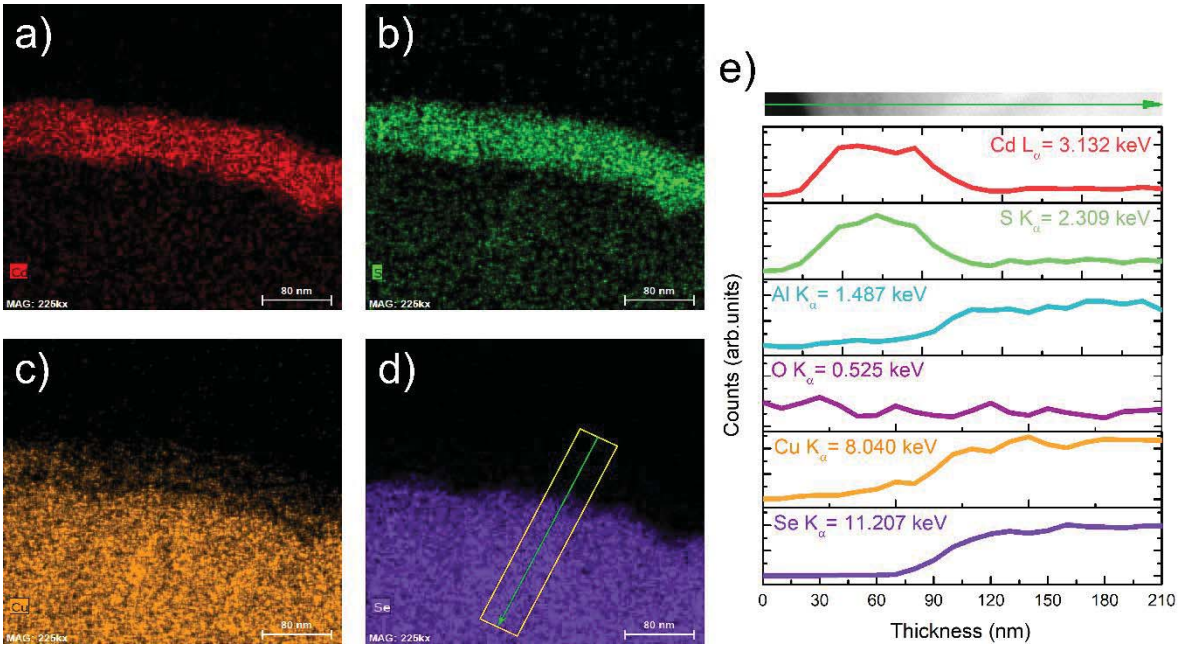

Fig. 6: STEM-EDS elemental mapping of the Al_2O_3/CdS sample. Full EDS mapping of a) Cd, b) S, c) Cu, and d) S, e). the EDS line profiles for Cd, S, Al, O, Cu and Se elements. The green arrow corresponds to the EDS linescan region.

Since the STEM/EDS analyses for the Al_2O_3/CdS sample did not reveal the presence of any element ascribed to the Al_2O_3 layer, several XPS measurements after etching down to the interface region were performed. For simplicity we will be calling this analysis a depth profile XPS. The depth profile started on the CdS, defined by the zero etch level (Fig. 7 a)) and finished in a depth level where both CdS and CIGS elements were found, defined as the level 4 of etching (Fig. 7 a)). It should be mentioned that Fig. 7 a) does not represent the elemental distribution of all elements of the depth profile process. XPS measurements in the energy range of the core-level of Al 2s (110 to 127 eV) were acquired during the etch process and the measurement at the etch level 4 (shown in Fig. 7 b)) revealing only the contributions of Auger Se, Cu 3s and In 4s [64,65]. No contribution from Al 2s was detected in any of the etch levels. We also note that even if Al could not be seen due to some superimposition, the O contribution lowers monotonically towards the CIGS with no maximum present. Hence, the XPS analysis is another evidence in favour of the absence of the Al_2O_3 layer in the Al_2O_3/CdS sample. It should also be noticed that the Cu 3s peak has a binding energy of 121.6 eV, which corresponds to CuS [66] being another factor that indicate that the Al 2s spectrum was taken on the interface region between CdS and CIGS as it is widely known that surface intermixing of only a few atoms might occur [50,61–63].

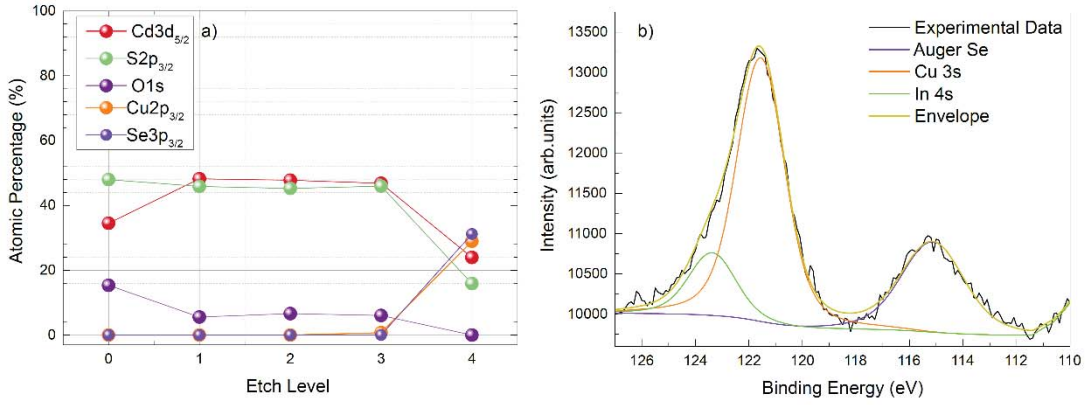

Fig. 7. a) XPS depth profile of the sample Al_2O_3/CdS, b) XPS spectra obtained on the interface between CIGS(/Al_2O_3)/CdS in the range of the energy of Al 2s spectra.

3.2 Optoelectronic Characterization

Metal-Insulator-Semiconductor (MIS) based C-V measurements were performed to extract the fixed insulator charges (Q_f) and the density of interface defects (D_{it}), which are present in the interface between the Al_2O_3 layer and the CIGS. A detailed procedure description to extract both parameters is described elsewhere [16]. The estimated Q_f values (Table 4) for the $Al_2O_3$50 and $Al_2O_3$250 samples are -11x10^9 and -7x10^9 cm^{-2}, respectively, indicating the existence of negative charge on the surface of the dielectric layer. The Q_f values obtained in this study are significantly different than the ones obtained in previous studies and show different polarity [16,67]. While a fine analysis of these values should be taken with care, the orders of magnitude can be compared. Relating the growth conditions of the passivation layers from this study with the ones from literature, all the Al_2O_3 films were growth by ALD, but at different temperatures. In this study, the Al_2O_3 growth was performed at 100 ºC, being 200 ºC and 300 ºC the temperatures of choice in Cunha *et al.* and Kotipalli *et al.*, respectively. For a growth temperature of 200 ºC, the obtained Q_f value was +4.1 x 10^{11} cm^{-2} and for 300 ºC, the authors obtained values between +8.1 and +33 x 10^{11} cm^{-2}. However, in [68] an Al_2O_3 film with negative polarity deposited at 250 ºC on CIGS was also reported, with a Q_f value around 10^{12} cm^{-2}. This last result indicates that, besides the deposition temperature, other parameters may be responsible for such polarity discrepancies. The time of exposition to the precursor and/or purge the precursors from the chamber may also change the Al_2O_3 film polarity, since Al_2O_3 may have a negative or positive polarity depending whether the film has an O excess or deficit, respectively [69]. Furthermore, the CIGS surface properties may also play an important role. For example, although the CIGS of this study and Cunha *et al.* are from the same baseline, those CIGS samples were protected with a CdS layer before the deposition of the Al_2O_3 layer. The deposition and subsequent removal of the CdS layer, may have changed the CIGS surface properties, leading to Al_2O_3 films with different fixed charge polarities. Hence, there are several growth parameters that need to be adapted accordingly, in order to obtain the required polarity. Nonetheless, the results from CIGS coming from the same baseline – this study, Cunha *et al.* and Kotipalli *et al* - suggest a correlation between the growth temperature and the Q_f value. Such trend is compatible with the one obtained in MIS structures based on Silicon by J. Buckley *et al.* There, the authors fixed the film thickness and varied the growth temperature for the Al_2O_3 layer, concluding that the higher the growth temperature, the higher the Q_f value [70]. However, more detailed studies that also include different CIGS are needed for a confirmation.

The obtained average D_{it} values (Table 4) for the samples $Al_2O_3$50 and $Al_2O_3$250 are 1.5 x 10^{11} and 3 x 10^{11} eV^{-1} cm^{-2}, respectively. Significantly different values are obtained when comparing the $Al_2O_3$50 D_{it} with a sample from the Kotipalli *et al.* study, which has the same thickness, but with a different growth temperature. On their study, they obtained a D_{it} value of (1.2-3.4) x 10^{12} eV^{-1} cm^{-2} which is much higher value than the one found here, 3 x 10^{11} eV^{-1} cm^{-2}. This correlation may be an evidence that the temperature is a parameter that has an impact on the properties of the passivation layer, not only on the Q_f, but also on the D_{it} with an interesting trade-off: low ALD temperature seems to provide very low D_{it} values at a cost of also having very low Q_f values. We note that good passivation layers usually need both low D_{it} values and at the same time high Q_f values in order to create a strong electrical field. Therefore, the values found here might not provide for outstanding passivation properties.

Table 4. Estimated average and standard deviation values of Q_f and D_{it} for the Al_2O_3 layer obtained from MIS based on a CIGS/Al_2O_3 structure schematically represented.

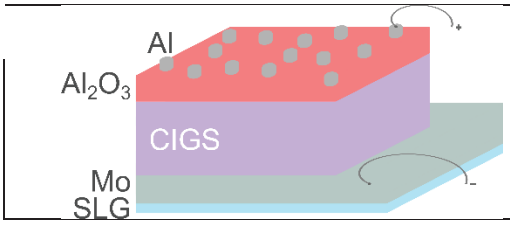

Sample	Q_f (cm^{-2})	D_{it} (eV^{-1} cm^{-2})
$Al_2O_3$50	(-11 ± 5) x 10^9	(1.5 ± 0.4) x 10^{11}
$Al_2O_3$250	(-7 ± 3) x 10^9	(3 ± 3) x 10^{11}

C-G-f measurements were performed in order to test different equivalent circuits of the ac response of the devices by performing a fitting to the measured data. A detailed description to select the most suitable circuit for each sample is described elsewhere [71]. All the samples demonstrate the same equivalent circuit (Fig. 8), each with three nodes, theoretically representing a different cell section of the device stack or interface. From the bottom to the top of the circuit, the first node represents the rear contact, Mo, the middle node represents the CIGS depletion layer [72], and the last one, the front interface. In order to ascribe the node to a layer, the capacitance and resistance values were considered and compared between samples. To distinguish between the nodes of the rear contact and

the CIGS depletion region, the capacitance and resistance values of each node were analysed. The node associated to the rear contact has higher capacitance and lower resistance values, than the ones obtained for the CIGS layer, due to the ohmic contact created between the $MoSe_2$ and the CIGS [73,74]. The CIGS depletion region node reflects the C_d capacitance and a parallel R_d resistance associated to the depletion region created by the semiconductor/front layer. We note that both in p-n junctions and in MIS devices, such C_d is expected [72]. In the previous node in parallel, a capacitance C_1 and a resistance R_1 in series is present, which may correspond to CIGS defects localized on the quasi-neutral region [71,75,76]. Taking into account the C_d capacitance values of the $Al_2O_3$50 and $Al_2O_3$250 samples, and comparing them with Ref and Al_2O_3/CdS, the Al_2O_3 samples show a higher C_d value, indicating a thinner CIGS depletion region, which is expected since there is no formation of a typical p-n junction. The existence of a C_d element in the Al_2O_3 samples, is related with the fixed charge density of the dielectric [72]. Such charge in the surface of the insulator layer will induce a small electrical field seen by these measurements as a capacity [71]. Comparing the Ref sample and the Al_2O_3/CdS one, all the individual electronic components have similar values, compatible with the nonexistence of the Al_2O_3 layer in the Al_2O_3/CdS sample. Since these two samples have a conventional pn-junction, a node with only a resistance (R_{front}) was expected, in opposition to the obtained node of a capacitance in parallel with a resistance. The need of an additional capacitance (C_{front}) suggests an inefficient contact between the CdS and the Al contact, leading to charge collection problems. Typical circuit fitting analysis with the ZnO:Al layer allow for good carrier extraction and this branch is no longer needed to achieve good fitting results [71,77]. For the case of the $Al_2O_3$50 and $Al_2O_3$250 samples, it was expected a front node with only a capacitance, representing the ideal insulator layer [72]. However, the model required an additional R_{front} resistance, compatible with possible shunts paths that may be present in the insulator. Comparing both Al_2O_3 samples, the values of the individual electronic component are very different between them, suggesting different optoelectronic properties in the two Al_2O_3 studied layers.

It is possible to calculate the theoretical capacitance (C) of the front layer, considering the relative dielectric permeability (ε_r) of 9 for Al_2O_3 and 8.9 for CdS [78,79], the area (A) of the MIS structures, the thickness (d) of the Al_2O_3 or CdS as previous determined, and the 8.85 x 10^{-12} F/m value for dielectric permittivity ε_0.

$$C = \frac{A\varepsilon_0\varepsilon_r}{d} \quad (1)$$

The d values correspond to front layer thickness estimated in the STEM images. The calculated values are presented in Table 5.

Table 5. Theoretical capacitance values calculated with the thickness obtained from TEM images of all samples. The experimental values are taken from the circuit fitting and they correspond to average and standard deviations values.

Sample name	Number of analysed devices	Theoretical estimated C_{front} (nF/cm^2)	Experimentally estimated C_{front} (nF/cm^2)
Ref	6	146	91 ± 33
$Al_2O_3$50	3	3190	73 ± 25
$Al_2O_3$250	5	354	399 ± 199
Al_2O_3/CdS	4	146	93 ± 24

In order to corroborate the circuit analyses done, the theoretical capacitance value was calculated and compared with the C_{front} values obtained from the respective circuit. Considering Table 5, the Ref and the Al_2O_3/CdS sample, have similar capacitance values - approximately 100 nF/cm^2 - close to the theoretical values. Looking to the $Al_2O_3$250 sample, the obtained theoretical capacitance value is 354 nF/cm^2, which is also in good agreement with the experimentally obtained by circuit fitting (399 nF/cm^2). However, the theoretical value calculated for the $Al_2O_3$50 sample is much higher than the value obtained from the fitted circuit, which may be due to the introduction of some impurities in the growing process of Al_2O_3, to the poor crystal quality of this layer, or to a non-conformality/uniformity of the layer. The comparison of the theoretical capacitance with the equivalent experimental values strongly supports the circuit analysis. The circuit fitting supports the absence of Al_2O_3 on the Al_2O_3/CdS.

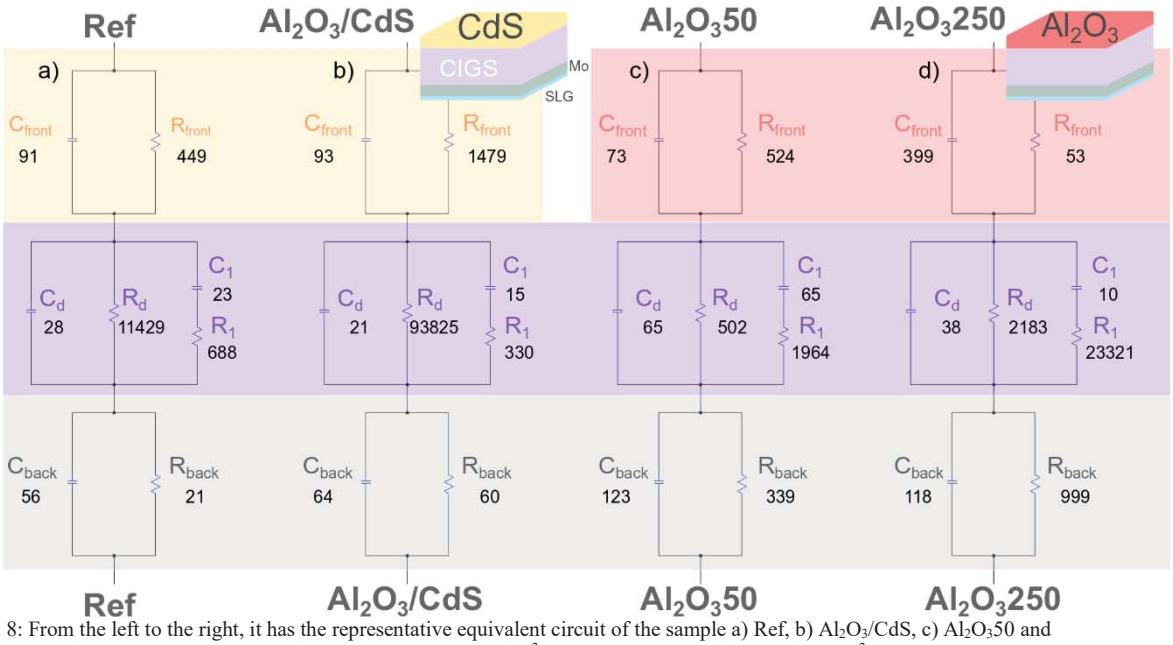

Fig. 8: From the left to the right, it has the representative equivalent circuit of the sample a) Ref, b) Al_2O_3/CdS, c) $Al_2O_3$50 and $Al_2O_3$250. The values of capacitance show on circuit are in nF/cm^2 and the resistance values are in Ω.cm^2.

The PL analysis gives important insights concerning the radiative and non-radiative electronic recombination. Low temperature PL spectra of all samples are shown in Fig. 9 a). The energy range and shape of the luminescence are close to observations in previous studies for Cu-poor CIGS samples with a linear Ga-profile, despite the front layer used over the CIGS [48,80]. The PL spectra measured with 16 mW are dominated by a radiative transition at approximately 1.04 -1.05 eV and a transition at approximately 1.00 eV with a lower relative intensity. This latter component has a higher relative impact in the $Al_2O_3$50 sample. The signal-to-noise ratio of the Al_2O_3/CdS PL spectrum is significantly lower, even considering an excitation power of 130 mW, which is ~8x higher than the 16 mW used to measure the remaining samples. The spectra of the Al_2O_3/CdS sample is broader, but to a great extent follows the shape of the remaining samples. However, a third transition may be present at higher energies. Due to the higher excitation power needed to be used in the Al_2O_3/CdS sample measurements, the spectrum is shifted to higher energies. The shift follows the expected blue shift of the peak energy with the increase of the excitation power, usually observed in highly doped and compensated semiconductors, such as CIGS [81,82]. The evaluation of the peak energy strongly depends on the excitation power, so the peak energy of all spectrum are not significantly different to be ascribed to electronic changes in the samples [81,82]. On the other hand, the low signal-to-noise ratio of the Al_2O_3/CdS PL spectrum is compatible with a higher density of defects that create non-radiative de-excitation channels in the CIGS layer. In this sample, Raman analysis showed differences between the CdS layer over the reference sample, as well as it was shown by GIXRD that its surface was different from the other samples. Hence, these observed changes play a role in the optoelectronic surface quality as demonstrated by the low PL signal-to-noise ratio.

TRPL decay of all samples is shown in Fig. 9 b). Different models were tested, and a double exponential function makes the best fit to all the experimental data of all samples:

$$I = A_1 e^{\frac{t}{\tau_1}} + A_2 e^{\frac{t}{\tau_2}} \quad (2).$$

Where I corresponds to the luminescence intensity, t is the acquisition time, τ_1 and τ_2 correspond to the fast and slow component of the TRPL decay lifetime, A_1 and A_2 are the corresponding pre-exponential factor. While there is not a full understanding of TRPL dynamics in complex semiconductors, several studies associate τ_1 with either interface recombination or to charge separation and τ_2 to bulk recombination [83–87]. The Ref and Al_2O_3/CdS samples have similar τ_1 values, 9.20 and 9.76 ns, respectively, indicating that the same dominant mechanism is quenching the TRPL decay. The similar τ_1 values also indicate from an optoelectronic point of view, that for the Ref and Al_2O_3/CdS samples, the front interfaces are equivalent. This similar value also suggests that τ_1 may be governed by the field effect of the p-n junction it will separate the charge carriers allowing for a higher τ_1 value than the ones obtained for the samples with the Al_2O_3 layer. The electrical field created by the Q_f of Al_2O_3 is much weaker than the one created by the pn-junction and, in this study, it will repel the minority charge from the interface of CIGS, due to the negative Q_f values. The τ_1 values obtained for the $Al_2O_3$50 and $Al_2O_3$250 samples

were 6.74 and 7.76 ns, respectively. From the C-V measurements, it is known that the $Al_2O_3$50 sample has a slightly higher negative Q_f value than the one of the $Al_2O_3$250 sample. Hence, this physical property will lead to a less efficient charge separation for $Al_2O_3$50 that is compatible with a lower τ_1 value obtained in this samples, comparing to the $Al_2O_3$250 one. So, from a charge separation point of view, τ_1 agrees with the previous measurements: the CdS samples have a higher efficiency of charge separation due to the p-n electrical field, than the one of the Al_2O_3 samples. For the Al_2O_3 samples, the one with the highest negative Q_f value will lead to an electrical field that promotes recombination also leading to the lowest τ_1 value. The τ_2 value is linked to bulk recombination, and with different values, it suggests some electronic changes in CIGS bulk of the samples. Ref (~73 ns) and $Al_2O_3$250 (65 ns) present quite similar τ_2 values where the $Al_2O_3$50 sample (55 ns) has a lower value that could be coming from this layer not showing a good conformal Al_2O_3 layer allowing oxygen to diffuse to the CIGS lowering its optoelectronic properties. The sample with the lowest τ_2 value is the Al_2O_3/CdS (47 ns), which may be an indication of differences in the structural and optoelectronic properties over the other three samples. The PL results for this sample are compatible with a higher density of efficient non-radiative recombination channels that will reduce the diffusion length of charge carriers, than the TRPL decay lifetime. The deposition of the Al_2O_3/CdS layers over the CIGS had the most harmful impact in the optoelectronic properties of the CIGS layer, in accordance to the previous analyses that demonstrated crystalline differences

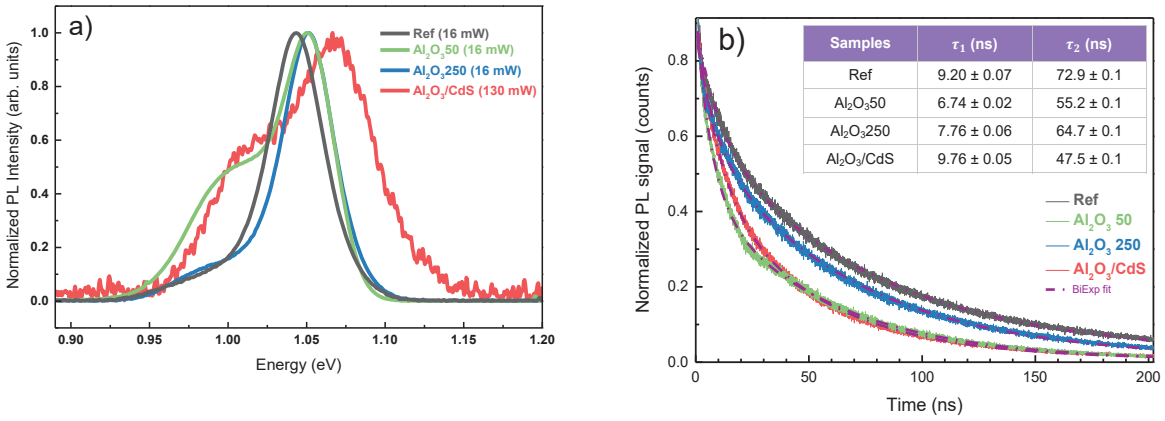

Fig. 9: Normalized PL spectra for all studied sample measured at ~7 K under an excitation power of 130 mW for sample Al_2O_3/CdS and 16 mW for the remaining samples. The signal-to-noise ratio is significantly lower for the PL spectrum of the Al_2O_3/CdS sample. Two radiative recombination are visible for all samples. TRPL decay of all studied samples fitted with a bi-exponential model (purple dash line). In the studied samples the τ_1 and τ_2 values reflect charge separation effect and bulk recombination, respectively.

In Low energy Muon Spin Spectroscopy (Low Energy μSR) positive muons are implanted in the sample at a depth that is controlled by varying the muon implantation energy in the range 2 - 24 keV. The muon signal is quite sensitive to the interaction of muons with electrons, thus affecting the final observed diamagnetic fraction, making it a powerful microscopic tool to probe the presence of defects and local electrical fields [88–90]. The behaviour of the muon diamagnetic fraction as a function of the sample depth inside CIGS layer (x) is shown in Fig. 10 for all the studied samples including a bare CIGS sample from the same batch. From the analysis of the muon spin spectroscopy spectra, it is possible to extract directly the diamagnetic fraction as a function of the muon implantation energy. In order to obtain the diamagnetic fraction as a function of the sample depth, a program developed by A. Simões *et al.*, was used [91]. The method requires performing Monte Carlo simulations using the TRIMP.SP code to obtain the muon stopping profile in the sample [92]. In Fig. 10, x=0 corresponds to the CIGS film surface, as seen by the muon probe. Therefore, region A is a region outside CIGS, which is relevant only for samples containing layers on top of CIGS. Since each material has its own characteristic diamagnetic fraction, it is possible to estimate the thickness of the different layers, which are compatible with the ones obtained through the TEM images (Table 3). Considering the bare CIGS sample, the behaviour of the diamagnetic fraction shows two distinct regions, B and C. Region C is the bulk region, whereas region B is a region close to the surface where the diamagnetic fraction is characterized by a well, which has been attributed to a surface defect layer at

CIGS [88,93]. The results for the $Al_2O_3$50 sample are similar to the results of the bare CIGS sample (except for a very slight decrease of the depth well in region B), indicating that the 4 nm thickness of Al_2O_3 layer has a minimal impact in the CIGS properties as detected by μSR. When comparing the Ref sample with the bare CIGS sample in region (B), it is visible a significant reduction of the CIGS surface defect layer by the CdS, namely by reducing both depth and width of the well. Comparing the $Al_2O_3$250 sample with the Ref and bare CIGS samples in region B, the Al_2O_3 produces a similar effect to the CdS, but it is less effective, since the reduction of the well width and depth are both smaller that observed in the Ref sample. μSR results suggest that the Al_2O_3 layer does have a beneficial impact in the CIGS surface defect region, although less effective than the CdS layer - which is well known to have a beneficial passivation effect on the CIGS surface [80]. However, comparing Al_2O_3/CdS with the Ref sample, the width of the interface region with defects is similar to the bare CIGS, although the depth of the well is similar to the Ref sample. Therefore, the μSR results suggest that the deposition of the thin Al_2O_3 layer between CdS and CIGS has a harmful impact on the CIGS properties, being in agreement with previous observations.

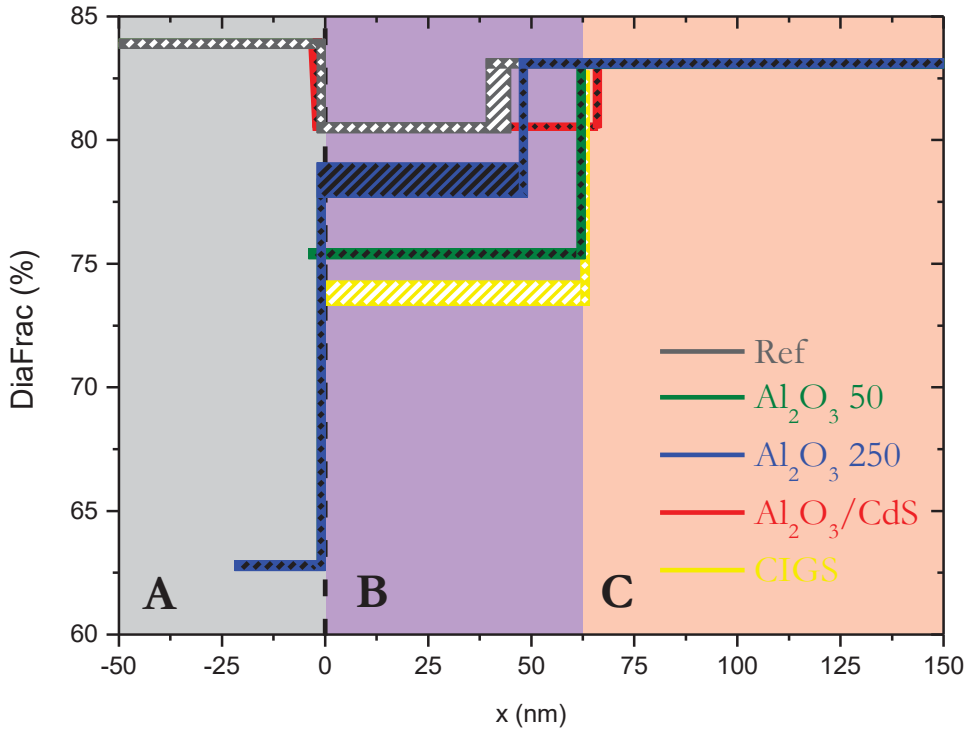

Fig. 10: Diamagnetic fraction of the μSR signal as a function of the position, x, inside CIGS film as a function of the muon implementation depth. The beginning of the CIGS surface, as seen by the muon probe, was defined as x=0. Note that the muons were implanted from the left side, which in this graph corresponds to a negative x. The thickness of the lines indicates the uncertainties in the parameters. Region A is the layer (or layers) on top of CIGS, region B is the CIGS region close to the surface and region C is CIGS bulk.

4. Discussion

The impact of depositing Al_2O_3 on CIGS was evaluated, in terms of optoelectronic properties, interface and bulk structural properties of CIGS. Raman Spectroscopy and GIXRD indicate that depositing Al_2O_3 alone is a harmless process to CIGS. From the Raman Spectroscopy, Ref and Al_2O_3/CdS samples reveal a different shape to the symmetry CdS peak, which is an indication of different structural properties of the CdS layer. The GIXRD reveals different preferential crystal reflectivity to the Al_2O_3/CdS sample, comparing with the samples that only contain

Al_2O_3. XRD shows similar crystal orientations for all samples. It can be concluded that the growth of CdS layer on Al_2O_3 changes the CIGS surface structural properties.

STEM-EDS analysis, reveals that the layer of Al_2O_3 is well defined. However for the Al_2O_3/CdS sample, neither the STEM-EDS nor the XPS analysis showed the presence of Al_2O_3. The inexistence of the Al_2O_3 in the sample Al_2O_3/CdS, may be related with the occurrence of a chemical attack by the ammonia present in the CBD used to grow the CdS layer. Kaige G. Sun *et al.* showed that are two major factors that may promote the etching of the Al_2O_3 in a basic bath: temperature (20 ° C and 60 ° C) and pH (9-12) [94]. In this study, the CdS was deposited at 60 ºC and pH 11 [49], which are conditions that should promote Al_2O_3 etching. Hence, in the Ref sample, the CdS growth occurs strictly on the CIGS surface, whereas in sample Al_2O_3/CdS it is a two steps process, first the Al_2O_3 layer is etched away, and then, the CdS layer starts its deposition process on the CIGS surface. Such process definitely causes changes to the CIGS and/or CdS as it was observed by Raman and XRD. Such etch process has already been reported in the literature, but for front passivation of Cu_2ZnSnS_4 based solar cells [95]. In that work it was also shown by STEM-EDS and XPS analysis that the Al_2O_3 can be etched away during the CBD of CdS. To reinforce this etch, substrates of Silicon, coated with Al_2O_3, with 10 nm of thickness, were dipped in an ammonia solution during 15 minutes and the layer was completely etched way, confirming that the layer is attacked by a solution with high pH.

The electrical measurements allowed to extract Q_f and D_{it} values. The D_{it} values obtained in this study have a low magnitude, indicating that the Al_2O_3 grown at 100 ºC, performs a good chemical passivation. However the Q_f values are also low and with the undesired polarity, for the insulator layer to perform the desired field-effect passivation, of the front layer, i.e. to repel minority carriers of this contact – holes -, and to attract majority carriers of this contact – electrons [96]. From the circuit matching it is possible to confirm some of the mentioned evidences. The values obtained of C_{front} are similar to Ref and Al_2O_3/CdS samples, which further confirms the inexistence of Al_2O_3 for the Al_2O_3/CdS sample and the values of C_d are similar, which indicates that the depletion region width is also similar. The samples that only contain Al_2O_3 have a C_d value higher than the previous samples, which indicates that there is a small depletion region, likely generated by the Q_f present at the interface. In equilibrium, the presence of the fixed negative charges on the insulator will act as an electrical field leading to charge motion. Another obtained result indicates that the Al_2O_3 appears to have different properties, due to the C_{front} values obtained to characterize such layer. The thinner Al_2O_3 layer does not have the same properties as the thicker one indicating that thicker layers might be needed to achieve good crystal quality. From the PL results, to obtain a reasonable signal-to-noise ratio spectrum for the Al_2O_3/CdS, it was necessary to apply a much higher excitation power, which indicates the presence of higher density of non-radiative recombination channels. From the TRPL measurements, the best fit used to the experimental data was a bi-exponential function where τ_1 was associated to charge separation. Ref and Al_2O_3/CdS present similar τ_1 values and are higher that the Al_2O_3 samples because the CdS creates a strong depletion region. Once again, the Q_f will promote a small electrical field that will create a weak charge separation as demonstrated by the low τ_1 values of these samples. τ_2 was associated to the bulk recombination. The Al_2O_3/CdS sample presented the lower τ_1 value, which is in conformity with the weak PL emission evidencing that the Al_2O_3 etch process might have caused detrimental processes such as elemental diffusion into the CIGS.

Muon spin spectroscopy reveals the impact of the introduction of CdS and Al_2O_3, comparing with a bare CIGS. There are two parameters that can be compared between samples, the depth and the width of a well. Such well has been attributed to surface defect region. These results show an interesting correlation with those obtained by TRPL (Fig. 9 b)):1) the well width in region B (Fig. 10) correlates with τ_2 in TRPL (Fig. 9 b) that is associated to bulk defects, - the lower the τ_2, the more defects are present in the bulk; 2) the well depth in region B (Fig. 10) correlates with τ_1 in TRPL (Fig. 9 b)) and it is associated to charge separation effect. So, the well depth follows the same trend of τ_1 and the well width tendency follows τ_2 suggesting that the muon analysis might also be sensitive to charge separation and to recombination effects. This is the first time that such correlation is found in μSR for complex semiconductors highlighting the importance of this technique and to the need to increase its understanding

In general, the use of Al_2O_3 does not seem to be beneficial when used with CdS as it promotes several problems and moreover it is etched away. A precise elemental diffusion of this sample such as Secondary ion mass spectrometry (SIMS) would help to understand if Al or any other element is being incorporated into the CIGS changing its properties. It is likely that an Al_2O_3 thicker layer could be deposited so that a control over the etching time could allow some residual layer to be present. Nonetheless, this would be a difficult process. However, the

Al_2O_3 alone does present good results in terms of not changing significantly the CIGS surface and bulk structural properties, and it also tends to keep the CIGS recombination channels the same as the ones when using CdS (as seen by PL). Hence, such material can be optimized to be used with alternative buffer layers that are already deposited by ALD.

5. Conclusions

In this work, the impact of depositing Al_2O_3 on CIGS was studied, with the purpose of evaluating the potential of this layer to be used as a front passivation material. The Al_2O_3 low temperature ALD process does not cause surface or bulk damage to the CIGS. This study shows that: i) the CIGS is kept with a low density of defects, ii) it does not change profoundly, or even it keeps the same, CIGS recombination channels, iii) CIGS crystalline properties are kept the same. CdS is not advised to be deposited on top of the Al_2O_3 as this latter layer is etched away during the basic CBD process and it also leads to severe degradation of the CIGS optoelectronic and surprisingly of the crystalline properties. Hence, Al_2O_3 will work best in conjugation with alternative buffer layers that do not require chemical bath depositions.

These results indicate the positive impact of using Al_2O_3 as a front passivation layer, which could be used in a new architecture for CIGS solar cells. The use of Al_2O_3 as a tunnelling layer on CIGS, with alternative buffers layers, which are less hazardous, have the potential for high performing CIGS interfaces, allowing for the use of other buffer layers and increasing, at the same time, the light to power conversion of the final devices.

Acknowledgments:

This work was supported in part by NovaCell (028075) and InovSolarCells (029696) and in part by Fundação para a Ciência e a Tecnologia and the ERDF through COMPETE2020. Fundação para a Ciência e a Tecnologia (FCT) is further acknowledged through IF/00133/2015, PD/BD/142780/2018 and SFRH/BD/146776/2019. The European Union's Horizon 2020 research and innovation programme ARCIGS-M project (Grant agreement 720887) is also acknowledged. The financial support by National Funds through the FCT - Fundação para a Ciência e a Tecnologia, I.P., under the scope of the projects UIDB/50025/2020 and UIDP/50025/2020 – Programático, are acknowledged. W. C. thanks the individual grant financed by the SusPhotoSolutions project CENTRO-01-0145-FEDER-000005. P. A. Fernandes would like to acknowledge FCT for the support of the project FCT UIDB/04730/2020. This work was supported with funds from FEDER (Programa Operacional Factores de Competitividade COMPETE) and from FCT [Fundação para a Ciência e Tecnologia (Portugal)] under Projects No. UID/FIS/04564/2016 and No. PTDC/FIS-MAC/29696/2017. The muon experiments were performed at the Swiss Muon Source SμS, Paul Scherrer Institute, Villigen, Switzerland.

References

[1] CIGS White Paper 2019 now available, (n.d.). https://cigs-pv.net/cigs-white-paper-2019-now-available/ (accessed April 30, 2020).

[2] M. Nakamura, K. Yamaguchi, Y. Kimoto, Y. Yasaki, T. Kato, H. Sugimoto, Cd-Free Cu(In,Ga)(Se,S)$_2$ Thin-Film Solar Cell With Record Efficiency of 23.35%, IEEE J. Photovoltaics. 9 (2019) 1863–1867. https://doi.org/10.1109/JPHOTOV.2019.2937218.

[3] B. Vermang, V. Fjällström, J. Pettersson, P. Salomé, M. Edoff, Development of rear surface passivated Cu(In,Ga)Se$_2$ thin film solar cells with nano-sized local rear point contacts, Sol. Energy Mater. Sol. Cells. 117 (2013) 505–511. https://doi.org/10.1016/j.solmat.2013.07.025.

[4] B. Vermang, V. Fjallstrom, X. Gao, M. Edoff, Improved Rear Surface Passivation of Cu(In,Ga)Se$_2$ Solar Cells: A Combination of an Al_2O_3 Rear Surface Passivation Layer and Nanosized Local Rear Point Contacts, IEEE J. Photovoltaics. 4 (2014) 486–492. https://doi.org/10.1109/JPHOTOV.2013.2287769.

[5] B. Vermang, J.T. Wätjen, V. Fjällström, F. Rostvall, M. Edoff, R. Kotipalli, F. Henry, D. Flandre, Employing Si solar cell technology to increase efficiency of ultra-thin Cu(In,Ga)Se$_2$ solar cells, Prog. Photovoltaics Res. Appl. 22 (2014) 1023–1029. https://doi.org/10.1002/pip.2527.

[6] P.M.P. Salomé, B. Vermang, R. Ribeiro-Andrade, J.P. Teixeira, J.M. V. Cunha, M.J. Mendes, S. Haque, J. Borme, H. Águas, E. Fortunato, R. Martins, J.C. González, J.P. Leitão, P.A. Fernandes, M. Edoff, S. Sadewasser, Passivation of Interfaces in Thin Film Solar Cells: Understanding the Effects of a Nanostructured Rear Point Contact Layer, Adv. Mater. Interfaces. 5 (2018) 1701101. https://doi.org/10.1002/admi.201701101.

[7] J. Löckinger, S. Nishiwaki, B. Bissig, G. Degutis, Y.E. Romanyuk, S. Buecheler, A.N. Tiwari, The use of HfO_2 in a point contact concept for front interface passivation of Cu(In,Ga)Se_2 solar cells, Sol. Energy Mater. Sol. Cells. 195 (2019) 213–219. https://doi.org/10.1016/j.solmat.2019.03.009.

[8] F. Werner, B. Veith-Wolf, M. Melchiorre, F. Babbe, J. Schmidt, S. Siebentritt, Ultra-thin passivation layers in Cu(In,Ga)Se_2 thin-film solar cells: full-area passivated front contacts and their impact on bulk doping, Sci. Rep. 10 (2020) 7530. https://doi.org/10.1038/s41598-020-64448-9.

[9] A. Chirilă, P. Reinhard, F. Pianezzi, P. Bloesch, A.R. Uhl, C. Fella, L. Kranz, D. Keller, C. Gretener, H. Hagendorfer, D. Jaeger, R. Erni, S. Nishiwaki, S. Buecheler, A.N. Tiwari, Potassium-induced surface modification of Cu(In,Ga)Se_2 thin films for high-efficiency solar cells, Nat. Mater. 12 (2013) 1107–1111. https://doi.org/10.1038/nmat3789.

[10] P. Jackson, R. Wuerz, D. Hariskos, E. Lotter, W. Witte, M. Powalla, Effects of heavy alkali elements in Cu(In,Ga)Se_2 solar cells with efficiencies up to 22.6%, Phys. Status Solidi - Rapid Res. Lett. 10 (2016) 583–586. https://doi.org/10.1002/pssr.201600199.

[11] P. Reinhard, B. Bissig, F. Pianezzi, E. Avancini, H. Hagendorfer, D. Keller, P. Fuchs, M. Döbeli, C. Vigo, P. Crivelli, S. Nishiwaki, S. Buecheler, A.N. Tiwari, Features of KF and NaF Postdeposition Treatments of Cu(In,Ga)Se_2 Absorbers for High Efficiency Thin Film Solar Cells, Chem. Mater. 27 (2015) 5755–5764. https://doi.org/10.1021/acs.chemmater.5b02335.

[12] P. Reinhard, F. Pianezzi, B. Bissig, A. Chirila, P. Blosch, S. Nishiwaki, S. Buecheler, A.N. Tiwari, Cu(In,Ga)Se_2 Thin-Film Solar Cells and Modules—A Boost in Efficiency Due to Potassium, IEEE J. Photovoltaics. 5 (2015) 656–663. https://doi.org/10.1109/JPHOTOV.2014.2377516.

[13] G. Yin, M. Song, S. Duan, P. Manley, D. Greiner, C.A. Kaufmann, M. Schmid, Well-Controlled Dielectric Nanomeshes by Colloidal Nanosphere Lithography for Optoelectronic Enhancement of Ultrathin Cu(In,Ga)Se_2 Solar Cells, ACS Appl. Mater. Interfaces. 8 (2016) 31646–31652. https://doi.org/10.1021/acsami.6b10135.

[14] T.S. Lopes, J.M. V. Cunha, S. Bose, J.R.S. Barbosa, J. Borme, O. Donzel-Gargand, C. Rocha, R. Silva, A. Hultqvist, W.-C. Chen, A.G. Silva, M. Edoff, P.A. Fernandes, P.M.P. Salome, Rear Optical Reflection and Passivation Using a Nanopatterned Metal/Dielectric Structure in Thin-Film Solar Cells, IEEE J. Photovoltaics. 9 (2019) 1421–1427. https://doi.org/10.1109/JPHOTOV.2019.2922323.

[15] N. Naghavi, F. Mollica, J. Goffard, J. Posada, A. Duchatelet, M. Jubault, F. Donsanti, A. Cattoni, S. Collin, P.P. Grand, J.J. Greffet, D. Lincot, Ultrathin Cu(In,Ga)Se_2 based solar cells, Thin Solid Films. 633 (2017) 55–60. https://doi.org/10.1016/j.tsf.2016.11.029.

[16] J.M. V. Cunha, P.A. Fernandes, A. Hultqvist, J.P. Teixeira, S. Bose, B. Vermang, S. Garud, D. Buldu, J. Gaspar, M. Edoff, J.P. Leitao, P.M.P. Salome, Insulator Materials for Interface Passivation of Cu(In,Ga)Se_2 Thin Films, IEEE J. Photovoltaics. 8 (2018) 1313–1319. https://doi.org/10.1109/JPHOTOV.2018.2846674.

[17] R. Kotipalli, O. Poncelet, G. Li, Y. Zeng, L.A. Francis, B. Vermang, D. Flandre, Addressing the impact of rear surface passivation mechanisms on ultra-thin Cu(In,Ga)Se_2 solar cell

performances using SCAPS 1-D model, Sol. Energy. 157 (2017) 603–613. https://doi.org/10.1016/j.solener.2017.08.055.

[18] J. Lontchi, M. Zhukova, M. Kovacic, J. Krc, W.-C. Chen, M. Edoff, S. Bose, P.M.P. Salome, J. Goffard, A. Cattoni, L. Gouillart, S. Collin, V. Gusak, D. Flandre, Optimization of Back Contact Grid Size in Al_2O_3-Rear-Passivated Ultrathin CIGS PV Cells by 2-D Simulations, IEEE J. Photovoltaics. (2020) 1–10. https://doi.org/10.1109/JPHOTOV.2020.3012631.

[19] A. Laemmle, R. Wuerz, M. Powalla, Efficiency enhancement of Cu(In,Ga)Se_2 thin-film solar cells by a post-deposition treatment with potassium fluoride, Phys. Status Solidi - Rapid Res. Lett. 7 (2013) 631–634. https://doi.org/10.1002/pssr.201307238.

[20] T. Lepetit, S. Harel, L. Arzel, G. Ouvrard, N. Barreau, KF post deposition treatment in co-evaporated Cu(In,Ga)Se_2 thin film solar cells: Beneficial or detrimental effect induced by the absorber characteristics, Prog. Photovoltaics Res. Appl. 25 (2017) 1068–1076. https://doi.org/10.1002/pip.2924.

[21] S. Siebentritt, E. Avancini, M. Bär, J. Bombsch, E. Bourgeois, S. Buecheler, R. Carron, C. Castro, S. Duguay, R. Félix, E. Handick, D. Hariskos, V. Havu, P. Jackson, H. Komsa, T. Kunze, M. Malitckaya, R. Menozzi, M. Nesladek, N. Nicoara, M. Puska, M. Raghuwanshi, P. Pareige, S. Sadewasser, G. Sozzi, A.N. Tiwari, S. Ueda, A. Vilalta-Clemente, T.P. Weiss, F. Werner, R.G. Wilks, W. Witte, M.H. Wolter, Heavy Alkali Treatment of Cu(In,Ga)Se_2 Solar Cells: Surface versus Bulk Effects, Adv. Energy Mater. 10 (2020) 1903752. https://doi.org/10.1002/aenm.201903752.

[22] T.-Y. Lin, I. Khatri, J. Matsuura, K. Shudo, W.-C. Huang, M. Sugiyama, C.-H. Lai, T. Nakada, Alkali-induced grain boundary reconstruction on Cu(In,Ga)Se_2 thin film solar cells using cesium fluoride post deposition treatment, Nano Energy. 68 (2020) 104299. https://doi.org/10.1016/j.nanoen.2019.104299.

[23] R. Carron, S. Nishiwaki, T. Feurer, R. Hertwig, E. Avancini, J. Löckinger, S. Yang, S. Buecheler, A.N. Tiwari, Advanced Alkali Treatments for High-Efficiency Cu(In,Ga)Se_2 Solar Cells on Flexible Substrates, Adv. Energy Mater. 9 (2019) 1900408. https://doi.org/10.1002/aenm.201900408.

[24] I. Khatri, T. Yashiro, T.-Y. Lin, M. Sugiyama, T. Nakada, Metastable Behavior on Cesium Fluoride-Treated Cu(In_{1-x},Ga_x)Se_2 Solar Cells, Phys. Status Solidi – Rapid Res. Lett. 14 (2020) 1900701. https://doi.org/10.1002/pssr.201900701.

[25] J.M. Raguse, C.P. Muzzillo, J.R. Sites, L. Mansfield, Effects of Sodium and Potassium on the Photovoltaic Performance of CIGS Solar Cells, IEEE J. Photovoltaics. 7 (2017) 303–306. https://doi.org/10.1109/JPHOTOV.2016.2621343.

[26] P.M.P. Salomé, H. Rodriguez-Alvarez, S. Sadewasser, Incorporation of alkali metals in chalcogenide solar cells, Sol. Energy Mater. Sol. Cells. 143 (2015) 9–20. https://doi.org/10.1016/j.solmat.2015.06.011.

[27] P. Jackson, D. Hariskos, R. Wuerz, O. Kiowski, A. Bauer, T.M. Friedlmeier, M. Powalla, Properties of Cu(In,Ga)Se_2 solar cells with new record efficiencies up to 21.7%, Phys. Status Solidi - Rapid Res. Lett. 9 (2015) 28–31. https://doi.org/10.1002/pssr.201409520.

[28] T.M. Friedlmeier, P. Jackson, A. Bauer, D. Hariskos, O. Kiowski, R. Wuerz, M. Powalla, Improved Photocurrent in Cu(In,Ga)Se_2 Solar Cells: From 20.8% to 21.7% Efficiency with CdS Buffer and 21.0% Cd-Free, IEEE J. Photovoltaics. 5 (2015) 1487–1491. https://doi.org/10.1109/JPHOTOV.2015.2458039.

[29] F. Pianezzi, P. Reinhard, A. Chirilă, B. Bissig, S. Nishiwaki, S. Buecheler, A.N. Tiwari, Unveiling the effects of post-deposition treatment with different alkaline elements on the electronic properties of CIGS thin film solar cells, Phys. Chem. Chem. Phys. 16 (2014) 8843. https://doi.org/10.1039/c4cp00614c.

[30] S.A. Jensen, S. Glynn, A. Kanevce, P. Dippo, J. V. Li, D.H. Levi, D. Kuciauskas, Beneficial effect of post-deposition treatment in high-efficiency Cu(In,Ga)Se_2 solar cells through reduced potential fluctuations, J. Appl. Phys. 120 (2016) 063106. https://doi.org/10.1063/1.4960344.

[31] L.M. Mansfield, R. Noufi, C.P. Muzzillo, C. DeHart, K. Bowers, B. To, J.W. Pankow, R.C. Reedy, K. Ramanathan, Enhanced Performance in Cu(In,Ga)Se_2 Solar Cells Fabricated by the Two-Step Selenization Process With a Potassium Fluoride Postdeposition Treatment, IEEE J. Photovoltaics. 4 (2014) 1650–1654. https://doi.org/10.1109/JPHOTOV.2014.2354259.

[32] T. Kohl, N.A. Rivas, J. de Wild, D.G. Buldu, G. Birant, G. Brammertz, M. Meuris, F.U. Renner, J. Poortmans, B. Vermang, Inclusion of Water in Cu(In, Ga)Se_2 Absorber Material During Accelerated Lifetime Testing, ACS Appl. Energy Mater. 3 (2020) 5120–5125. https://doi.org/10.1021/acsaem.0c00610.

[33] C.P. Muzzillo, J.D. Poplawsky, H.M. Tong, W. Guo, T. Anderson, Revealing the beneficial role of K in grain interiors, grain boundaries, and at the buffer interface for highly efficient $CuInSe_2$ solar cells, Prog. Photovoltaics Res. Appl. 26 (2018) 825–834. https://doi.org/10.1002/pip.3022.

[34] S. Shimakawa, Y. Hashimoto, S. Hayashi, T. Satoh, T. Negami, Annealing effects on $Zn_{1-x}Mg_xO$/CIGS interfaces characterized by ultraviolet light excited time-resolved photoluminescence, Sol. Energy Mater. Sol. Cells. 92 (2008) 1086–1090. https://doi.org/10.1016/j.solmat.2008.03.014.

[35] T. Kobayashi, K. Yamauchi, T. Nakada, Comparison of cell performance of ZnS(O,OH)/CIGS solar cells with UV-assisted MOCVD-ZnO:B and sputter-deposited ZnO:Al window layers, in: 2012 IEEE 38th Photovolt. Spec. Conf. PART 2th</sup> Photovolt. Spec. Conf. PART 2, IEEE, 2012: pp. 1–6. https://doi.org/10.1109/PVSC-Vol2.2012.6656753.

[36] X. Cui, K. Sun, J. Huang, J.S. Yun, C.-Y. Lee, C. Yan, H. Sun, Y. Zhang, C. Xue, K. Eder, L. Yang, J.M. Cairney, J. Seidel, N.J. Ekins-Daukes, M. Green, B. Hoex, X. Hao, Cd-Free Cu_2ZnSnS_4 solar cell with an efficiency greater than 10% enabled by Al_2O_3 passivation layers, Energy Environ. Sci. 12 (2019) 2751–2764. https://doi.org/10.1039/C9EE01726G.

[37] G. Sozzi, S. Di Napoli, R. Menozzi, B. Bissig, S. Buecheler, A.N. Tiwari, Impact of front-side point contact/passivation geometry on thin-film solar cell performance, Sol. Energy Mater. Sol. Cells. 165 (2017) 94–102. https://doi.org/10.1016/j.solmat.2017.02.031.

[38] M. Nerat, Copper–indium–gallium–selenide (CIGS) solar cells with localized back contacts for achieving high performance, Sol. Energy Mater. Sol. Cells. 104 (2012) 152–158. https://doi.org/10.1016/j.solmat.2012.05.020.

[39] G. Birant, J. de Wild, M. Meuris, J. Poortmans, B. Vermang, Dielectric-Based Rear Surface Passivation Approaches for Cu(In,Ga)Se_2 Solar Cells—A Review, Appl. Sci. 9 (2019) 677. https://doi.org/10.3390/app9040677.

[40] S. Choi, Y. Kamikawa, J. Nishinaga, A. Yamada, H. Shibata, S. Niki, Lithographic fabrication of point contact with Al_2O_3 rear-surface-passivated and ultra-thin Cu(In,Ga)Se_2 solar cells, Thin Solid Films. 665 (2018) 91–95. https://doi.org/10.1016/j.tsf.2018.08.044.

[41] M. Sugiyama, H. Sakakura, S.-W. Chang, M. Itagaki, Investigation of Sputtering Damage

around pn Interfaces of Cu(In,Ga)Se_2 Solar Cells by Impedance Spectroscopy, Electrochim. Acta. 131 (2014) 236–239. https://doi.org/10.1016/j.electacta.2014.04.058.

[42] N. Naghavi, S. Spiering, M. Powalla, B. Cavana, D. Lincot, High-efficiency copper indium gallium diselenide (CIGS) solar cells with indium sulfide buffer layers deposited by atomic layer chemical vapor deposition (ALCVD), Prog. Photovoltaics Res. Appl. 11 (2003) 437–443. https://doi.org/10.1002/pip.508.

[43] T. Törndahl, E. Coronel, A. Hultqvist, C. Platzer-Björkman, K. Leifer, M. Edoff, The effect of $Zn_{1-x}Mg_xO$ buffer layer deposition temperature on Cu(In,Ga)Se_2 solar cells: A study of the buffer/absorber interface, Prog. Photovoltaics Res. Appl. 17 (2009) 115–125. https://doi.org/10.1002/pip.859.

[44] P.M.P. Salomé, J. Keller, T. Törndahl, J.P. Teixeira, N. Nicoara, R.-R. Andrade, D.G. Stroppa, J.C. González, M. Edoff, J.P. Leitão, S. Sadewasser, CdS and $Zn_{1-x}Sn_xO_y$ buffer layers for CIGS solar cells, Sol. Energy Mater. Sol. Cells. 159 (2017) 272–281. https://doi.org/10.1016/j.solmat.2016.09.023.

[45] J. Sterner, J. Malmström, L. Stolt, Study on ALD In_2S_3/Cu(In,Ga)Se_2 interface formation, Prog. Photovoltaics Res. Appl. 13 (2005) 179–193. https://doi.org/10.1002/pip.595.

[46] A. Shimizu, S. Chaisitsak, T. Sugiyama, A. Yamada, M. Konagai, Zinc-based buffer layer in the Cu(InGa)Se_2 thin film solar cells, Thin Solid Films. 361–362 (2000) 193–197. https://doi.org/10.1016/S0040-6090(99)00792-0.

[47] T. Nam, J.-M. Kim, M.-K. Kim, H. Kim, W.-H. Kim, Low-temperature Atomic Layer Deposition of TiO_2, Al_2O_3, and ZnO Thin Films, J. Korean Phys. Soc. 59 (2011) 452–457. https://doi.org/10.3938/jkps.59.452.

[48] J.P. Teixeira, R.B.L. Vieira, B.P. Falcão, M. Edoff, P.M.P. Salomé, J.P. Leitão, Recombination Channels in Cu(In,Ga)Se_2 Thin Films: Impact of the Ga-Profile, J. Phys. Chem. C. 124 (2020) 12295–12304. https://doi.org/10.1021/acs.jpcc.0c02622.

[49] J. Lindahl, U. Zimmermann, P. Szaniawski, T. Torndahl, A. Hultqvist, P. Salome, C. Platzer-Bjorkman, M. Edoff, Inline Cu(In,Ga)Se_2 Co-evaporation for High-Efficiency Solar Cells and Modules, IEEE J. Photovoltaics. 3 (2013) 1100–1105. https://doi.org/10.1109/JPHOTOV.2013.2256232.

[50] P.M.P. Salome, R. Ribeiro-Andrade, J.P. Teixeira, J. Keller, T. Torndahl, N. Nicoara, M. Edoff, J.C. Gonzalez, J.P. Leitao, S. Sadewasser, Cd and Cu Interdiffusion in Cu(In, Ga)Se_2 /CdS Hetero-Interfaces, IEEE J. Photovoltaics. 7 (2017) 858–863. https://doi.org/10.1109/JPHOTOV.2017.2666550.

[51] T. Prokscha, E. Morenzoni, K. Deiters, F. Foroughi, D. George, R. Kobler, A. Suter, V. Vrankovic, The new beam at PSI: A hybrid-type large acceptance channel for the generation of a high intensity surface-muon beam, Nucl. Instruments Methods Phys. Res. Sect. A Accel. Spectrometers, Detect. Assoc. Equip. 595 (2008) 317–331. https://doi.org/10.1016/j.nima.2008.07.081.

[52] S. Roy, P. Guha, S.N. Kundu, H. Hanzawa, S. Chaudhuri, A.K. Pal, Characterization of Cu(In,Ga)Se_2 films by Raman scattering, Mater. Chem. Phys. 73 (2002) 24–30. https://doi.org/10.1016/S0254-0584(01)00345-5.

[53] J. Bi, L. Yao, J. Ao, S. Gao, G. Sun, Q. He, Z. Zhou, Y. Sun, Y. Zhang, Pulse electro-deposition of copper on molybdenum for Cu(In,Ga)Se_2 and $Cu_2ZnSnSe_4$ solar cell applications, J. Power Sources. 326 (2016) 211–219. https://doi.org/10.1016/j.jpowsour.2016.07.005.

[54] K.K. Nanda, S.N. Sarangi, S.N. Sahu, S.K. Deb, S.N. Behera, Raman spectroscopy of CdS nanocrystalline semiconductors, Phys. B Condens. Matter. 262 (1999) 31–39. https://doi.org/10.1016/S0921-4526(98)00474-8.

[55] C.-H. Chen, C.-H. Hsu, C.-Y. Chien, Y.-H. Wu, C.-H. Lai, A straightforward method to prepare chalcopyrite CIGS films by one-step sputtering process without extra Se supply, in: 2011 37th IEEE Photovolt. Spec. Conf., IEEE, 2011: pp. 002687–002690. https://doi.org/10.1109/PVSC.2011.6186502.

[56] Y. Cho, D.-W. Kim, S. Ahn, D. Nam, H. Cheong, G.Y. Jeong, J. Gwak, J.H. Yun, Recombination in Cu(In,Ga)Se_2 thin-film solar cells containing ordered vacancy compound phases, Thin Solid Films. 546 (2013) 358–361. https://doi.org/10.1016/j.tsf.2013.04.078.

[57] S. Gieraltowska, L. Wachnicki, B.S. Witkowski, R. Mroczynski, P. Dluzewski, M. Godlewski, Characterization of dielectric layers grown at low temperature by atomic layer deposition, Thin Solid Films. 577 (2015) 97–102. https://doi.org/10.1016/j.tsf.2015.01.059.

[58] V. Miikkulainen, M. Leskelä, M. Ritala, R.L. Puurunen, Crystallinity of inorganic films grown by atomic layer deposition: Overview and general trends, J. Appl. Phys. 113 (2013) 021301. https://doi.org/10.1063/1.4757907.

[59] International centre for diffraction data, PDF: 04-007-4441, (n.d.).

[60] P.M.P. Salomé, V. Fjällström, P. Szaniawski, J.P. Leitão, A. Hultqvist, P.A. Fernandes, J.P. Teixeira, B.P. Falcão, U. Zimmermann, A.F. da Cunha, M. Edoff, A comparison between thin film solar cells made from co-evaporated $CuIn_{1-x}Ga_xSe_2$ using a one-stage process versus a three-stage process, Prog. Photovoltaics Res. Appl. 23 (2015) 470–478. https://doi.org/10.1002/pip.2453.

[61] T. Nakada, A. Kunioka, Direct evidence of Cd diffusion into Cu(In, Ga)Se_2 thin films during chemical-bath deposition process of CdS films, Appl. Phys. Lett. 74 (1999) 2444–2446. https://doi.org/10.1063/1.123875.

[62] D. Abou-Ras, G. Kostorz, A. Romeo, D. Rudmann, A.N. Tiwari, Structural and chemical investigations of CBD- and PVD-CdS buffer layers and interfaces in Cu(In,Ga)Se_2-based thin film solar cells, Thin Solid Films. 480–481 (2005) 118–123. https://doi.org/10.1016/j.tsf.2004.11.033.

[63] X. He, T. Paulauskas, P. Ercius, J. Varley, J. Bailey, G. Zapalac, D. Poplavskyy, N. Mackie, A. Bayman, D. Spaulding, R. Klie, V. Lordi, A. Rockett, Cd doping at PVD-CdS/$CuInGaSe_2$ heterojunctions, Sol. Energy Mater. Sol. Cells. 164 (2017) 128–134. https://doi.org/10.1016/j.solmat.2017.01.043.

[64] Y. Yuan, L. Zhang, G. Yan, G. Cen, Y. Liu, L. Zeng, C. Zeng, C. Zhao, R. Hong, W. Mai, Significantly Enhanced Detectivity of CIGS Broadband High-Speed Photodetectors by Grain Size Control and ALD-Al_2O_3 Interfacial-Layer Modification, ACS Appl. Mater. Interfaces. 11 (2019) 20157–20166. https://doi.org/10.1021/acsami.9b04248.

[65] B.V. Crist, Handbook of Monochromatic XPS Spectra: The Elements of Native Oxides, 2020.

[66] T.R.N. Kutty, A controlled copper-coating method for the preparation of ZnS: Mn DC electroluminescent powder phosphors, Mater. Res. Bull. 26 (1991) 399–406. https://doi.org/10.1016/0025-5408(91)90054-P.

[67] R. Kotipalli, B. Vermang, J. Joel, R. Rajkumar, M. Edoff, D. Flandre, Investigating the electronic properties of Al_2O_3/Cu(In,Ga)Se_2 interface, AIP Adv. 5 (2015) 107101. https://doi.org/10.1063/1.4932512.

[68] W.-W. Hsu, J.Y. Chen, T.-H. Cheng, S.C. Lu, W.-S. Ho, Y.-Y. Chen, Y.-J. Chien, C.W. Liu, Surface passivation of Cu(In,Ga)Se_2 using atomic layer deposited Al_2O_3, Appl. Phys. Lett. 100 (2012) 023508. https://doi.org/10.1063/1.3675849.

[69] J.R. Weber, A. Janotti, C.G. Van de Walle, Native defects in Al_2O_3 and their impact on III-V/Al_2O_3 metal-oxide-semiconductor-based devices, J. Appl. Phys. 109 (2011) 033715. https://doi.org/10.1063/1.3544310.

[70] J. Buckley, B. De Salvo, D. Deleruyelle, M. Gely, G. Nicotra, S. Lombardo, J.F. Damlencourt, P. Hollinger, F. Martin, S. Deleonibus, Reduction of fixed charges in atomic layer deposited Al_2O_3 dielectrics, Microelectron. Eng. 80 (2005) 210–213. https://doi.org/10.1016/j.mee.2005.04.070.

[71] J.M.V. Cunha, C. Rocha, C. Vinhais, P.A. Fernandes, P.M.P. Salome, Understanding the AC Equivalent Circuit Response of Ultrathin Cu(In,Ga)Se_2 Solar Cells, IEEE J. Photovoltaics. 9 (2019) 1442–1448. https://doi.org/10.1109/JPHOTOV.2019.2927918.

[72] S. M. Sze and K. K. Ng, Physics of Semiconductor Devices, Third Edit, 2017.

[73] K.-J. Hsiao, J.-D. Liu, H.-H. Hsieh, T.-S. Jiang, Electrical impact of $MoSe_2$ on CIGS thin-film solar cells, Phys. Chem. Chem. Phys. 15 (2013) 18174. https://doi.org/10.1039/c3cp53310g.

[74] T.-Y. Lin, T. Yashiro, I. Khatri, M. Sugiyama, Characterization on proton irradiation-damaged interfaces of CIGS-related multilayered compound semiconductors for solar cells by electrochemical impedance spectroscopy, Jpn. J. Appl. Phys. 59 (2020) 058003. https://doi.org/10.35848/1347-4065/ab891f.

[75] Y.Y. Proskuryakov, K. Durose, B.M. Taele, S. Oelting, Impedance spectroscopy of unetched CdTe/CdS solar cells—equivalent circuit analysis, J. Appl. Phys. 102 (2007) 024504. https://doi.org/10.1063/1.2757011.

[76] P.A. Fernandes, A.F. Sartori, P.M.P. Salomé, J. Malaquias, A.F. da Cunha, M.P.F. Graça, J.C. González, Admittance spectroscopy of Cu_2 $ZnSnS_4$ based thin film solar cells, Appl. Phys. Lett. 100 (2012) 233504. https://doi.org/10.1063/1.4726042.

[77] J.M. V. Cunha, C. Rocha, C. Vinhais, P.A. Fernandes, P.M.P. Salome, Equivalent Circuit For AC Response of Cu(In,Ga)Se_2 Thin Film Solar Cells, in: 2019 IEEE 46th Photovolt. Spec. Conf., IEEE, 2019: pp. 0923–0927. https://doi.org/10.1109/PVSC40753.2019.8980822.

[78] M.J. Biercuk, D.J. Monsma, C.M. Marcus, J.S. Becker, R.G. Gordon, Low-temperature atomic-layer-deposition lift-off method for microelectronic and nanoelectronic applications, Appl. Phys. Lett. 83 (2003) 2405–2407. https://doi.org/10.1063/1.1612904.

[79] W. Wondmagegn, I. Mejia, A. Salas-Villasenor, H.J. Stiegler, M.A. Quevedo-Lopez, R.J. Pieper, B.E. Gnade, CdS Thin Film Transistor for Inverter and Operational Amplifier Circuit Applications, Microelectron. Eng. 157 (2016) 64–70. https://doi.org/10.1016/j.mee.2016.02.042.

[80] P.M.P. Salome, J.P. Teixeira, J. Keller, T. Torndahl, S. Sadewasser, J.P. Leitao, Influence of CdS and ZnSnO Buffer Layers on the Photoluminescence of Cu(In,Ga)Se_2Thin Films, IEEE J. Photovoltaics. 7 (2017) 670–675. https://doi.org/10.1109/JPHOTOV.2016.2639347.

[81] J.P. Teixeira, R.A. Sousa, M.G. Sousa, A.F. da Cunha, P.A. Fernandes, P.M.P. Salomé, J.C. González, J.P. Leitão, Comparison of fluctuating potentials and donor-acceptor pair transitions in a Cu-poor Cu_2ZnSnS_4 based solar cell, Appl. Phys. Lett. 105 (2014) 163901. https://doi.org/10.1063/1.4899057.

[82] J.K. Larsen, K. Burger, L. Gutay, S. Siebentritt, Temperature dependence of potential fluctuations in chalcopyrites, in: 2011 37Th IEEE Photovolt. Spec. Conf., IEEE, 2011: pp. 000396–000401. https://doi.org/10.1109/PVSC.2011.6185978.

[83] I. Khatri, H. Fukai, H. Yamaguchi, M. Sugiyama, T. Nakada, Effect of potassium fluoride post-deposition treatment on Cu(In,Ga)Se_2 thin films and solar cells fabricated onto sodalime glass substrates, Sol. Energy Mater. Sol. Cells. 155 (2016) 280–287. https://doi.org/10.1016/j.solmat.2016.06.023.

[84] S. Nakatsuka, N. Yuzawa, J. Chantana, T. Minemoto, Y. Nose, Solar cells using bulk crystals of rare metal-free compound semiconductor $ZnSnP_2$, Phys. Status Solidi. 214 (2017) 1600650. https://doi.org/10.1002/pssa.201600650.

[85] S. Shimakawa, K. Kitani, S. Hayashi, T. Satoh, Y. Hashimoto, Y. Takahashi, T. Negami, Characterization of Cu(In,Ga)Se_2 thin films by time-resolved photoluminescence, Phys. Status Solidi. 203 (2006) 2630–2633. https://doi.org/10.1002/pssa.200669583.

[86] S.J. Heise, J.F. López Salas, Charge separation effects in time-resolved photoluminescence of Cu(In,Ga)Se_2 thin film solar cells, Thin Solid Films. 633 (2017) 35–39. https://doi.org/10.1016/j.tsf.2016.11.031.

[87] W.-H. Ho, C.-H. Hsu, T.-H. Yeh, Y.-H. Chang, S.-Y. Wei, T.-Y. Lin, C.-H. Lai, Room-Temperature Chemical Solution Treatment for Flexible ZnS(O,OH)/Cu(In,Ga)Se_2 Solar Cell: Improvements in Interface Properties and Metastability, ACS Appl. Mater. Interfaces. 8 (2016) 6709–6717. https://doi.org/10.1021/acsami.5b11028.

[88] H. V. Alberto, R.C. Vilão, R.B.L. Vieira, J.M. Gil, A. Weidinger, M.G. Sousa, J.P. Teixeira, A.F. da Cunha, J.P. Leitão, P.M.P. Salomé, P.A. Fernandes, T. Törndahl, T. Prokscha, A. Suter, Z. Salman, Slow-muon study of quaternary solar-cell materials: Single layers and *p* - *n* junctions, Phys. Rev. Mater. 2 (2018) 025402. https://doi.org/10.1103/PhysRevMaterials.2.025402.

[89] T. Prokscha, H. Luetkens, E. Morenzoni, G.J. Nieuwenhuys, A. Suter, M. Döbeli, M. Horisberger, E. Pomjakushina, Depth dependence of the ionization energy of shallow hydrogen states in ZnO and CdS, Phys. Rev. B. 90 (2014) 235303. https://doi.org/10.1103/PhysRevB.90.235303.

[90] J. Woerle, T. Prokscha, A. Hallén, U. Grossner, Interaction of low-energy muons with defect profiles in proton-irradiated Si and 4*H* - SiC, Phys. Rev. B. 100 (2019) 115202. https://doi.org/10.1103/PhysRevB.100.115202.

[91] A.F.A. Simões, H. V. Alberto, R.C. Vilão, J.M. Gil, J.M. V. Cunha, M.A. Curado, P.M.P. Salomé, T. Prokscha, A. Suter, Z. Salman, Muon implantation experiments in films: Obtaining depth-resolved information, Rev. Sci. Instrum. 91 (2020) 023906. https://doi.org/10.1063/1.5126529.

[92] E. Morenzoni, H. Glückler, T. Prokscha, R. Khasanov, H. Luetkens, M. Birke, E.M. Forgan, C. Niedermayer, M. Pleines, Implantation studies of keV positive muons in thin metallic layers, Nucl. Instruments Methods Phys. Res. Sect. B Beam Interact. with Mater. Atoms. 192 (2002) 254–266. https://doi.org/10.1016/S0168-583X(01)01166-1.

[93] E. Ribeiro, H. V. Alberto, R.C. Vilão, J.M. Gil, A. Weidinger, P.M.P. Salomé, T. Prokscha, A. Suter, Z. Salman, CdS versus ZnSnO buffer layers for a CIGS solar cell: a depth-resolved analysis using the muon probe, EPJ Web Conf. 233 (2020) 05004. https://doi.org/10.1051/epjconf/202023305004.

[94] K.G. Sun, Y. V. Li, D.B. Saint John, T.N. Jackson, pH-Controlled Selective Etching of Al_2O_3 over

ZnO, ACS Appl. Mater. Interfaces. 6 (2014) 7028–7031. https://doi.org/10.1021/am501912q.

[95] J. Park, J. Huang, J. Yun, F. Liu, Z. Ouyang, H. Sun, C. Yan, K. Sun, K. Kim, J. Seidel, S. Chen, M.A. Green, X. Hao, The Role of Hydrogen from ALD-Al_2O_3 in Kesterite Cu2ZnSnS4 Solar Cells: Grain Surface Passivation, Adv. Energy Mater. 8 (2018) 1701940. https://doi.org/10.1002/aenm.201701940.

[96] R. Brendel, R. Peibst, Contact Selectivity and Efficiency in Crystalline Silicon Photovoltaics, IEEE J. Photovoltaics. 6 (2016) 1413–1420. https://doi.org/10.1109/JPHOTOV.2016.2598267.